Chapter 17
The Capture/Emission Time Map Approach to the Bias Temperature Instability

Tibor Grasser

Abstract Recent results suggest that the bias temperature instability can in good approximation be understood as the collective response of an ensemble of independent defects. Although the kinetics of charge capture and defect creation clearly require the presence of charge carriers in the channel, they appear reaction rather than diffusion limited. While a number of peculiar features in these kinetics have been revealed recently, the most striking feature remains the wide distribution of reaction rates, or equivalently, time constants. By modeling the activation energies of the time constants via bivariate Gaussian distributions in what we call *capture/emission time maps*, a wide range of experimentally observed features can be explained in closed analytical form. Examples are the temperature- and bias-independent power-law time exponent during stress including saturation at longer times, the long logarithmic-like recovery traces, as well as differences and similarities between DC and AC stress.

17.1 Introduction

Numerous studies conducted over the last couple of decades have shown that at least two types of defects contribute to the bias temperature instability (BTI), namely oxide and interface defects [1–7]. Considerable evidence has piled up in recent years suggesting that oxide defects are mainly responsible for the recoverable component of BTI [8–11], while interface defects are mostly permanent in typical experimental windows [12–15].

Charge exchange between the channel and oxide defects has traditionally been modeled using a simple Shockley–Read–Hall (SRH) model [16]. The SRH model was originally developed for bulk defects, but later extended in an empirical manner

T. Grasser (✉)
TU Wien, Institute for Microelectronics, Gusshausstrasse 27-29, 1040 Wien, Austria
e-mail: grasser@iue.tuwien.ac.at

T. Grasser (ed.), *Bias Temperature Instability for Devices and Circuits*,
DOI 10.1007/978-1-4614-7909-3_17, © Springer Science+Business Media New York 2014

to describe oxide defects by the introduction of a WKB tunneling factor [17–20]. Detailed time-dependent defect spectroscopy (TDDS) studies have shown, however, that the oxide defects contributing to NBTI are of a more complicated nature [9, 10, 21, 22]. In particular, transitions between the different charge states are consistent with nonradiative multiphonon (NMP) processes, as has already been observed in random telegraph noise studies [23]. Furthermore, metastable states seem to be an essential aspect since they explain the switching trap behavior [10,21,24,25] as well as the frequency dependence of the capture time constant [26–30]. Nevertheless, the most intriguing feature appears to be the wide distribution of both the capture and the emission time constants [31]. These time constants may even be too short to be experimentally observable ($<1\,\mu$s) as well as extremely large (>1 ks). While the chemical nature of these oxide defects has not been unanimously identified [32–34], it is this distribution of time constants which essentially determines the typical recovery behavior of a device following bias temperature stress [31, 35–38].

Interface states, at least at SiO_2/Si interfaces, are most likely due to silicon dangling bonds at the silicon–insulator interface, known as P_b centers [33, 39, 40]. The creation dynamics are much harder to study experimentally since both capture and emission time constants are rather large. Also, in every BTI experiment the recoverable component R appears to overshadow the build-up of the permanent component P [15]. Thus, a number of attempts have been made at characterizing P:

- Application of measurement methods which (hopefully) dominantly measure interface states, such as charge-pumping techniques [13, 41–43].
- Attempts to remove R by for instance accelerating recovery by switching the gate voltage into accumulation.
- Attempts to guess from the dominant behavior of R on the underlying evolution of P (the *universal recovery* idea) [44, 45].

Unfortunately, all these methods introduce uncertainties:

- First, charge-pumping currents have to be converted to the typically measured threshold-voltage shifts used to characterize R to make the components comparable. However, it is not clear whether only interface states contribute to those recombination currents and how the density-of-states in the fraction of the bandgap visible to charge-pumping has to be extended to the remainder of the bandgap to allow for a meaningful comparison [15, 41, 46].
- Second, all attempts in removing R by the application of controlled discharge pulses appear to leave some unspecified remaining fraction of defects behind, since not all defects react to switches of the gate bias [24, 47]. Furthermore, the devices may show a tendency to go back to their pre-pulse rather than to their pre-stress state [15].
- Finally, while the universality appears to capture an interesting aspect of R, it is not clear what physical process is responsible for such a behavior and how accurate such an extraction scheme is.

As a consequence, we know much less about *P* than we know about *R*, making the available models more rudimentary. In particular, it remains controversial whether *R* and *P* are created in a coupled manner [48, 49] or not [11, 37, 50]. Nonetheless, similar to *R*, the creation/annealing time constants of *P* also show a wide distribution. This is also consistent with electron-spin-resonance data on creation and annealing of P_b centers [51].

Since the wide distribution of the time constants is responsible for both the build-up and the recovery of *R* and *P*, this distribution essentially determines the time-dependence of the degradation. As such, it appears natural to seek a description of BTI based on these distributions [31, 36–38]. A particularly useful observation in enabling a simple description is that despite their multi-state nature, charging and discharging of individual oxide traps responsible for *R* can be well described by an effective first-order process [20], at least for lower frequencies [29]. While not that much is known about *P*, available experimental data appear to indicate that the same is true for *P* [4, 28]. In the following we will summarize our recent attempts in developing such a model which describes the build-up of *R* and *P* as the collective action of a large number of individual defects, each described by a first-order process.

17.2 The Capture and Emission Times

In order to describe the defects, we first have to specify their capture and emission times as a function of bias and temperature. While the models used for oxide and interface traps are fundamentally different, they can still be approximately brought into the same mathematical form, yielding effective capture and emission times

$$\tau_c = \tau_0 e^{\beta \mathscr{E}_c} \quad \text{and} \quad \tau_e = \tau_0 e^{\beta \mathscr{E}_e} \tag{17.1}$$

with $\beta = 1/k_B T$, k_B the Boltzmann constant, and T the absolute temperature. In general, the effective time constant τ_0 will depend only weakly on bias and temperature, while the effective capture and emission barriers $\mathscr{E}_c$ and $\mathscr{E}_e$ can have a strong bias dependence. In the following, the assumptions required to bring available physical models for oxide and interface defects into the simple form (17.1) will be summarized.

17.2.1 Oxide Defects

We begin our discussion with oxide defects, which have been shown [10, 24, 29, 47] to have at least four states, 1, 1′, 2′, and 2, see Fig. 17.1. The unprimed states 1 and 2 are assumed to correspond to the stable equilibrium configuration in the neutral and positive charge states, while 1′ and 2′ are their metastable counterparts.

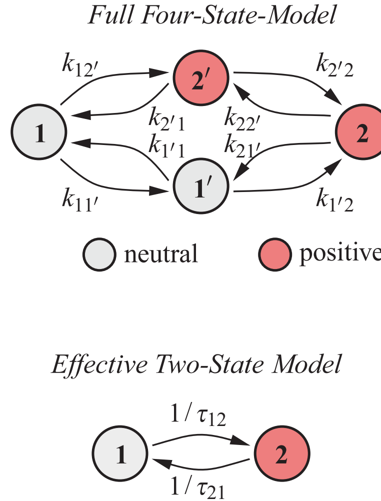

Fig. 17.1 *Top*: The four states of oxide defects extracted from DC TDDS experiments [10, 52]. Each defect has two stable states, 1 and 2, and possibly two metastable states 1′ and 2′. The metastable state 2′ seems to be always present, while the existence of the metastable state 1′ decides on whether the trap behaves like a fixed or a switching trap [24, 53]. *Bottom*: An effective two-state approximation of the four-state defect using the first-passage times τ_{12} and τ_{21} [10, 20]

The transitions between the states are described by 8 rates, k_{ij}. In a first-order description, we neglect the switching state 1′. This approximation is valid as long as the gate voltage remains above the threshold voltage but misses the rapid decrease of the emission time once the device is biased into depletion or accumulation [47]. Transitions between these states appear to be consistent with a Markov process, which in essence means that the defect forgets its past once it has arrived in a certain state. These transitions are stochastic processes, where the transition events for each individual transition are exponential distributed. The parameter of this distribution gives the mean transition time. Neglecting state 1′, the first passage times [54, 55] for an overall transition from 1 to 2 define the effective capture and emission times as [20]

$$\tau_c = \frac{k_{12'} + k_{2'1} + k_{2'2}}{k_{12'}\, k_{2'2}} \quad \text{and} \quad \tau_e = \frac{k_{2'2} + k_{22'} + k_{2'1}}{k_{22'}\, k_{2'1}}, \tag{17.2}$$

which is not quite in the simple form (17.1) yet. While the first passage times exactly describe the mean of the overall distribution of the capture and emission times, replacing the four-state defect model (or three-state model in this case) by an effective two-state model approximates the distributions of the stochastic capture and emission events by exponential distributions [20]. Nonetheless, this appears to be an excellent approximation [10].

The physics behind the initial charge capture transition $1 \to 2'$ can be modeled at various levels of detail. In order to obtain the simplest results possible, we consider only the ground state of the neutral and the metastable positive configuration (E_1 and $E_{2'}$) and assume that all holes are located at the valence band edge E_V directly at

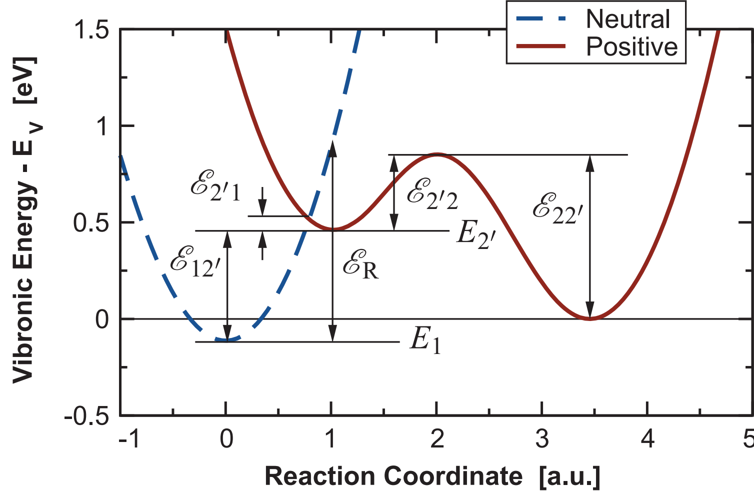

Fig. 17.2 Definition of the symbols required to describe the adiabatic defect potential of the simple model without the switching state $1'$. The vibronic energy, which is the sum of the electronic and vibrational energies, is shown relative to the substrate valence band in state 2, that is, $E_2 = 0$

the interface, see Fig. 17.2. The transitions are described using NMP theory [56–60] based on linear electron–phonon coupling [61], with the rates given in the classical (high-temperature) limit by

$$k_{12'} = p\, v_{\text{th}}\, \sigma\, \mathrm{e}^{-x/x_0}\, \mathrm{e}^{-\beta \mathscr{E}_{12'}}, \tag{17.3}$$

$$k_{2'1} = p\, v_{\text{th}}\, \sigma\, \mathrm{e}^{-x/x_0}\, \mathrm{e}^{-\beta \mathscr{E}_{12'}}\, \mathrm{e}^{-\beta E_{1\text{F}}}, \tag{17.4}$$

where p is the surface hole concentration, v_{th} the thermal velocity, σ the capture cross section, x_0 the parameter in the simplified WKB tunneling expression, and $E_{1\text{F}} = E_1 - E_\text{F}$ the distance of the trap level from the Fermi-level. For linear electron–phonon coupling the NMP barrier is obtained as

$$\mathscr{E}_{12'} = \frac{(\mathscr{E}_\text{R} + E_{2'1})^2}{4\mathscr{E}_\text{R}} \tag{17.5}$$

where $E_{2'1} = E_{2'} - E_1$, $\mathscr{E}_\text{R} = S\hbar\omega$ as the lattice relaxation energy, ω the oscillator frequency determined by the curvature of the parabolic adiabatic potential [62], and S the Huang–Rhys factor which gives the number of phonons required for the optical transition. For strong electron–phonon coupling ($\mathscr{E}_\text{R} \gg E_{2'1}$), the quadratic dependence simplifies to $\mathscr{E}_{12'} = \mathscr{E}_\text{R}/4 + E_{2'1}/2$, which we will use in the following for the derivation of the analytical results. It is convenient to express the flat-band defect energy levels E_{10} and $E_{2'0}$ relative to $E_{\text{V}0}$, the flat-band valence band edge, by introducing $\mathscr{E}_1 = E_{10} - E_{\text{V}0}$ and $\mathscr{E}_{2'} = E_{2'0} - E_{\text{V}0}$. Assuming to first order that the charges trapped inside the oxide have only a small impact on the electric field, we have $E_{2'1} = E_{2'0} - E_{10} - \mathrm{q}xF = \mathscr{E}_{2'} - \mathscr{E}_1 - \mathrm{q}xF$, with x the distance of the trap into the oxide, F the oxide field, and E_{i0} the trap level for $F = 0$. The sign conventions

are such that x is positive and F is positive for a negative bias at the gate (NBTI). Inserting the above into the rates delivers

$$k_{12'} = \quad p\, v_{\mathrm{th}}\, \sigma\, \mathrm{e}^{-x/x_0}\, \mathrm{e}^{-\beta(\mathscr{E}_{\mathrm{R}}+2\mathscr{E}_{2'})/4}\, \mathrm{e}^{+\beta(\mathscr{E}_1+\mathrm{q}xF)/2}, \tag{17.6}$$

$$k_{2'1} = N_{\mathrm{v}}\, v_{\mathrm{th}}\, \sigma\, \mathrm{e}^{-x/x_0}\, \mathrm{e}^{-\beta(\mathscr{E}_{\mathrm{R}}+2\mathscr{E}_{2'})/4}\, \mathrm{e}^{-\beta(\mathscr{E}_1+\mathrm{q}xF)/2}, \tag{17.7}$$

where Boltzmann statistics have been assumed for simplicity, $p = N_{\mathrm{v}}\exp(\beta E_{\mathrm{VF}})$. The barrier crossing rates for the transitions $2' \leftrightharpoons 2$ are expressed by a simple Arrhenius law with an attempt frequency $\nu = 10^{13}\,\mathrm{s}^{-1}$

$$k_{2'2} = \nu \mathrm{e}^{-\beta \mathscr{E}_{2'2}} \quad \text{and} \quad k_{22'} = \nu \mathrm{e}^{-\beta(\mathscr{E}_{2'2}+\mathscr{E}_{2'})}. \tag{17.8}$$

We proceed by rewriting the first passage times using the definitions $\tau_{ij} = 1/k_{ij}$ as

$$\tau_{\mathrm{c}} = \tau_{12'} + \tau_{2'2}\left(1+\frac{\tau_{12'}}{\tau_{2'1}}\right) = \tau_{12'} + \tau_{2'2}\left(1+\frac{N_{\mathrm{v}}}{p}\mathrm{e}^{-\beta(\mathscr{E}_1+\mathrm{q}xF)}\right), \tag{17.9}$$

$$\tau_{\mathrm{e}} = \tau_{22'} + \tau_{2'1}\left(1+\frac{\tau_{22'}}{\tau_{2'2}}\right) = \tau_{22'} + \tau_{2'1}\left(1+\mathrm{e}^{\beta \mathscr{E}_{2'}}\right). \tag{17.10}$$

This is an interesting result. (a) First, we see that τ_{c} at very high fields becomes bias independent and is only determined by the barrier between $2'$ and 2, $\tau_{\mathrm{c}} \approx \tau_{2'2}$. (b) Both time constants can potentially show a strong exponential bias dependence, via the dependence on $\tau_{12'}$ and $\tau_{2'1}$. (c) While both time constants $\tau_{12'}$ and $\tau_{2'1}$ depend on $\mathscr{E}_1$, this dependence is not normally relevant for τ_{e}, which is dominated by $\tau_{22'}$. (d) Finally, under typical NBTI conditions, recovery is measured at low F where $\tau_{2'1}$ is small, so $\tau_{\mathrm{e}} \approx \tau_{22'}$, that is, recovery is dominated by the barrier from 2 to $2'$. Only for biases lower than about the threshold voltage, the pathway $2 \leftrightharpoons 1' \to 1$ can be triggered when accessible (switching traps). As such hole emission even from below E_{V} will have a barrier since holes can no longer simply "bubble up" as in the SRH picture [20].

In principle, all parameters appearing in (17.9) and (17.10) are different for each defect, including the surface hole concentration p due to the random location of the current percolation paths [63, 64]. Unfortunately, not much is known at present about the nature of these distributions, so we have to invoke a few bold assumptions here: first, it has been demonstrated [65] that τ_{c} and x are uncorrelated for those defects contribution to RTN. Whether this also holds for NBTI is unknown at the moment, but we will nonetheless assume in the following $x = \bar{x}$, its average effective value. Lacking evidence to the contrary, all other parameters are assumed to follow a Gaussian distribution for simplicity. A particularly noteworthy issue is the following: since many parameters (e.g., $\mathscr{E}_{\mathrm{R}}$, $\mathscr{E}_1$, $\mathscr{E}_{2'}$) which control the defect behavior result from a certain defect constellation, it appears likely that some hidden correlations exist. Note also that for defects contributing to NBTI, $\mathscr{E}_1$ is typically smaller than zero, since the defect has to lie below the valence band to be initially neutral (to be more precise, the defect level has to lie below the Fermi-level at the read-out or recovery voltage).

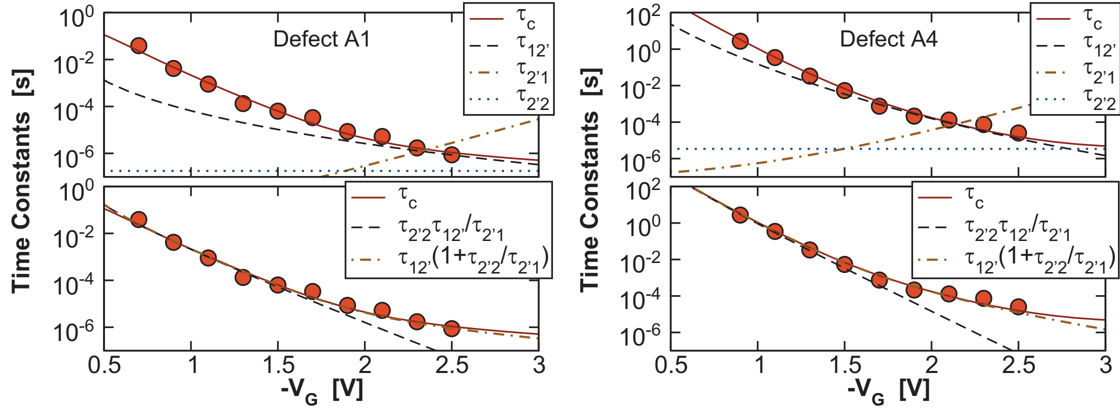

Fig. 17.3 The effective capture time τ_c is a function of all three partial rates. Shown are two defects from [10] together with a fit to the model

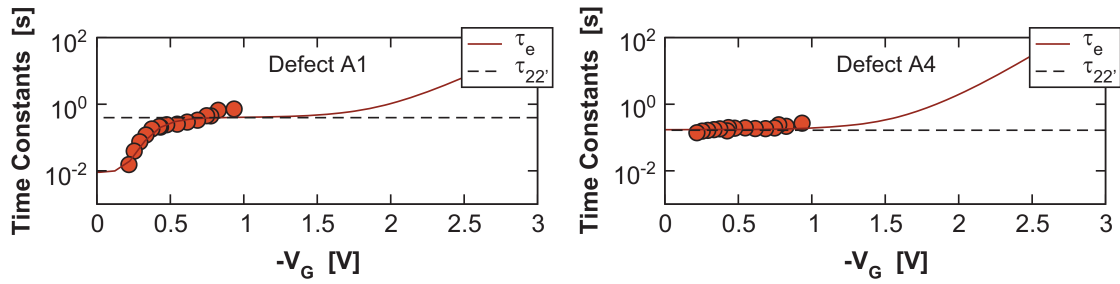

Fig. 17.4 The effective emission time τ_c is dominated by $\tau_{22'}$ for V_G above the threshold voltage. Shown are two defects from [10] together with a fit to the model. Defect A1 is a switching trap while the emission time of A4 appears independent of V_G. The switching behavior results from a backward transition via the pathway $2 \leftrightharpoons 1' \rightarrow 1$ but is ignored in the present discussion for simplicity. See [47] for an extended data set and modeling results toward lower V_G

17.2.1.1 Low Fields

For low fields during stress, Fig. 17.3 indicates that τ_c is dominated by the $\tau_{2'2}\tau_{12'}/\tau_{2'1}$ term, while Fig. 17.4 shows that τ_e is bias independent. Thus we have

$$\tau_c = \tau_{2'2}\frac{\tau_{12'}}{\tau_{2'1}} = \nu e^{-\beta(E_{VF}+\mathscr{E}_{2'2}+\mathscr{E}_1+q\bar{x}F)}, \tag{17.11}$$

$$\tau_e = \tau_{22'} \qquad = \nu e^{-\beta(\mathscr{E}_{2'2}+\mathscr{E}_{2'})} = \nu e^{-\beta\mathscr{E}_{22'}}. \tag{17.12}$$

As can be seen, τ_c depends exponentially on the electric field F. The above also implies that there is some explicit correlation between τ_c and τ_e due to the occurrence of $\mathscr{E}_{2'2}$ in both expressions in addition to the unknown hidden correlations in the parameters.

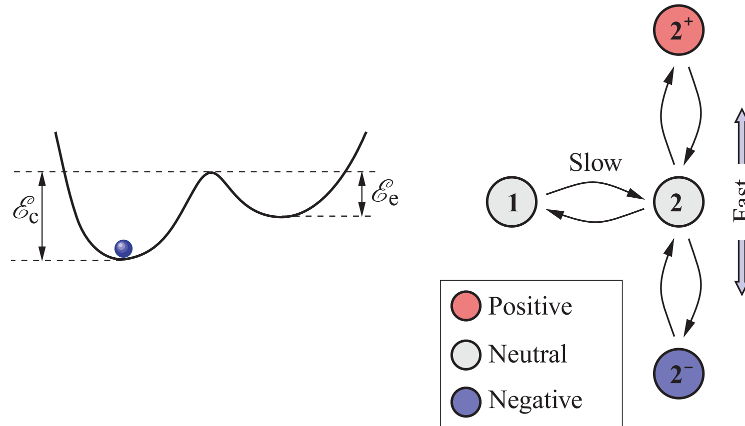

Fig. 17.5 *Left*: Simple double-well model used for the creation of interface states. *Right*: State diagram for interface states. The double-well model is used to describe the transitions $1 \rightleftharpoons 2$, while a change of the charge state can be obtained using a SRH model

17.2.1.2 Medium Fields

At medium stress fields, τ_c is basically given by $\tau_{12'}$ and we have $\tau_c = \tau_{12'}$ and $\tau_e = \tau_{22'}$. In this regime no obvious correlation exists and any experimentally observed correlation must be due to hidden correlations in the parameters. This issue is discussed in the next section using a simple model for the creation of the interface states.

17.2.1.3 Strong Fields

At strong fields, the capture time will be dominated by the bias-independent barrier $\mathscr{E}_{2'2}$ and thus become bias-independent. The emission time, on the other hand, will be dominated by the bias-dependent barrier $\mathscr{E}_{2'1}$ and increase significantly.

17.2.2 Interface Defects

Since inside typical measurement windows NBTI degradation is dominated by the activation and annealing of oxide defects, much less is known about interface states, the creation of which appears nonetheless universally acknowledged [11, 13, 37, 50, 66]. As the details of the creation dynamics are unclear at the moment, the creation of interface states from a precursor state 1 is typically modeled using a simple double-well model into the neutral state 2 [11, 37, 50, 67], see Fig. 17.5. Again, as with the hole trapping model, the barriers are assumed to be statistically distributed [4, 51, 67]. Alternatively, some groups advocate a reaction–diffusion mechanism [50, 68, 69], which we consider inadequate due to the lacking direct experimental

evidence [70] and additional theoretical difficulties [71,72]. The charge state of the amphoteric defect is then determined using an SRH model [73]. Since in this picture the charge state can change rapidly, we limit our attention to the creation process $1 \leftrightharpoons 2$. In the simple double-well model, we obtain the classical over-the-barrier rates

$$\tau_\mathrm{c} = \nu \mathrm{e}^{\beta \mathscr{E}_\mathrm{c}} \quad \text{and} \quad \tau_\mathrm{e} = \nu \mathrm{e}^{\beta \mathscr{E}_\mathrm{e}}. \tag{17.13}$$

As hinted at previously, we will study in the following the distributions of τ_c and τ_e for a large number of defects. Written in the form (17.13), no correlation between these two time constants would be obtained if $\mathscr{E}_\mathrm{c}$ and $\mathscr{E}_\mathrm{e}$ were independent random variables. However, given that the adiabatic potential describing the double-well is a result of the various forces acting on the atoms, such an independence is unlikely. Quite to the contrary, one can expect a hidden correlation between the parameters $\mathscr{E}_\mathrm{c}$ and $\mathscr{E}_\mathrm{e}$, since it is unlikely that changes in the defect configuration only impacts the barrier E_B without altering the levels E_1 and E_2. As such, if we choose to write $\mathscr{E}_\mathrm{c} = E_\mathrm{B} - E_1$ and $\mathscr{E}_\mathrm{e} = E_\mathrm{B} - E_2$, a distribution of E_B will affect both $\mathscr{E}_\mathrm{c}$ and $\mathscr{E}_\mathrm{e}$ since

$$\tau_\mathrm{c} = \nu \mathrm{e}^{\beta (E_\mathrm{B} - E_1)} \quad \text{and} \quad \tau_\mathrm{e} = \nu \mathrm{e}^{\beta (E_\mathrm{B} - E_2)} = \tau_\mathrm{c} \mathrm{e}^{\beta (E_1 - E_2)}. \tag{17.14}$$

Even in this case, the energies E_B, E_1, and E_2 cannot be expected to be independent. Nonetheless, to make the model even simpler, we assume that it is the quantities $E_\mathrm{B1} = E_\mathrm{B} - E_1$ and $E_{12} = E_1 - E_2$ that are independently distributed. The only justification we have at the moment is that this assumption appears to capture the essence of the experimental data, in particular the observed correlation between τ_c and τ_e.

17.3 The Capture/Emission Time Map

We now proceed from individual defects of either type to a large collection of both types. Assume we have a collection of independent defects with a distribution of capture and emission times. In the interval $[\tau_\mathrm{c}, \tau_\mathrm{c} + \mathrm{d}\tau_\mathrm{c}]$ and $[\tau_\mathrm{e}, \tau_\mathrm{e} + \mathrm{d}\tau_\mathrm{e}]$ the number of defects contributing to ΔV_th is $g(\tau_\mathrm{c}, \tau_\mathrm{e})\,\mathrm{d}\tau_\mathrm{c}\,\mathrm{d}\tau_\mathrm{e}$, where the capture/emission time distribution ("the map") g has dimension $\mathrm{V/s^2}$. Depending on the stressing history of the device, all defects with similar τ_c and τ_e values can be expected to have a similar occupancy. This occupancy, $h(\tau_\mathrm{c}, \tau_\mathrm{e})$, is 1 if all defects in that interval fully contribute to ΔV_th and 0 if they do not contribute at all. For the assumed first-order processes, h is simple to calculate as a consequence of arbitrarily switching gate voltages between a high and low level. Then, by multiplying h with g and integrating over the whole domain, ΔV_th can be calculated at any time, provided g remains constant. Apparently, this is roughly the case, although defect transformations have been occasionally observed [10,37,74–77], which will be neglected in the following.

Mathematically, the total ΔV_{th} is thus obtained by summing up the contributions of all defects with a particular combination of τ_{c} and τ_{e}, embodied by $g(\tau_{\mathrm{c}},\tau_{\mathrm{e}})\mathrm{d}\tau_{\mathrm{c}}\mathrm{d}\tau_{\mathrm{e}}$, weighted by the occupancy $h(\tau_{\mathrm{c}},\tau_{\mathrm{e}})$ as

$$\Delta V_{\mathrm{th}}(t_{\mathrm{s}},t_{\mathrm{r}}) \approx \int_0^\infty \mathrm{d}\tau_{\mathrm{c}} \int_0^\infty \mathrm{d}\tau_{\mathrm{e}}\, g(\tau_{\mathrm{c}},\tau_{\mathrm{e}})\, h(\tau_{\mathrm{c}},\tau_{\mathrm{e}};t_{\mathrm{s}},t_{\mathrm{r}}). \tag{17.15}$$

As said before, the occupancy function h depends on the history of stress and recovery cycles the device has been exposed to and on the details of the physical process. A simple case is obtained for a collection of defects following first-order processes, which have been subjected to a DC stress phase of duration t_{s} and a recovery time t_{r},

$$h(\tau_{\mathrm{c}},\tau_{\mathrm{e}};t_{\mathrm{s}},t_{\mathrm{r}}) = \left(1-\mathrm{e}^{-t_{\mathrm{s}}/\tau_{\mathrm{c}}}\right)\mathrm{e}^{-t_{\mathrm{r}}/\tau_{\mathrm{e}}} \tag{17.16}$$

provided that the occupancy is 0 at the initial read-out voltage and 1 after a stress duration $t_{\mathrm{s}} \gg \tau_{\mathrm{c}}$. Note that τ_{c} is taken at the stress voltage, while τ_{e} is considered at the recovery voltage. To simplify the integration, we employ the approximation

$$h(\tau_{\mathrm{c}},\tau_{\mathrm{e}};t_{\mathrm{s}},t_{\mathrm{r}}) \approx H(t_{\mathrm{s}}-\tau_{\mathrm{c}})H(\tau_{\mathrm{e}}-t_{\mathrm{r}}). \tag{17.17}$$

where H is the unit step function. Although this approximation is somewhat crude, as the two transitions contained in h cover a decade in time, it gives us a very simple and intuitive connection between ΔV_{th} and g,

$$\Delta V_{\mathrm{th}}(t_{\mathrm{s}},t_{\mathrm{r}}) \approx \int_0^{t_{\mathrm{s}}} \mathrm{d}\tau_{\mathrm{c}} \int_{t_{\mathrm{r}}}^\infty \mathrm{d}\tau_{\mathrm{e}}\, g(\tau_{\mathrm{c}},\tau_{\mathrm{e}}). \tag{17.18}$$

In words this means that ΔV_{th} is given by the sum of all defects charged until t_{s} but not yet discharged after t_{r}. Equation (17.18) can now be used to give a simple method for the extraction of g by simply taking the negative mixed partial derivative of a given ΔV_{th} stress/recovery data set [78],

$$g(\tau_{\mathrm{c}},\tau_{\mathrm{e}}) \approx -\frac{\partial^2 \Delta V_{\mathrm{th}}(\tau_{\mathrm{c}},\tau_{\mathrm{e}})}{\partial\tau_{\mathrm{c}}\,\partial\tau_{\mathrm{e}}}. \tag{17.19}$$

Note that completely permanent defects with $\tau_{\mathrm{e}} \to \infty$ do not show up in the CET map. Given the wide distribution of the defect time constants, it is advantageous to represent the CET map on logarithmic axes. Transformation of the variables gives [20]

$$\tilde{g}(\tau_{\mathrm{c}},\tau_{\mathrm{e}}) \approx -\frac{\partial^2 \Delta V_{\mathrm{th}}(\tau_{\mathrm{c}},\tau_{\mathrm{e}})}{\partial\log(\tau_{\mathrm{c}})\,\partial\log(\tau_{\mathrm{e}})} = \tau_{\mathrm{c}}\tau_{\mathrm{e}}\, g(\tau_{\mathrm{c}},\tau_{\mathrm{e}}). \tag{17.20}$$

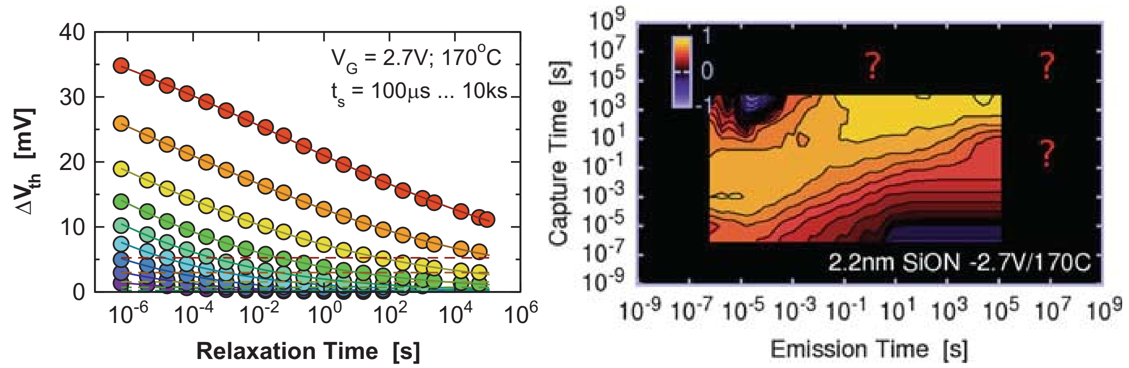

Fig. 17.6 *Left*: Experimental recovery data following increasing stress times (*symbols*). *Right*: The logarithmic CET map obtained by taking the numerical derivative of the data. Numerical integration results in the *solid lines* of the *left figure*. The *dashed lines* are obtained from a "permanent" component with $\tau_e > t_{relax,max}$, which is not directly available in the numerical CET map and has to be provided separately. The map is normalized and plotted using a signed log operator $\operatorname{sign}(g)\log_{10}(1+\kappa|g/g_{max}|)/\log_{10}(1+\kappa)$ with $\kappa = 100$ to bring out all important details

While g gives the density of defects per unit time, for example information on how much ΔV_{th} is gained/lost in a second, $\tilde{g}$ gives the density on a logarithmic scale, for example on how much ΔV_{th} is gained/lost per decade.

An example of $\tilde{g}$ extracted from experimental $\Delta V_{th}(t_s, t_r)$ data is shown in Fig. 17.6. Note that while a correlation between τ_c and τ_e exists, it is weak and a significant density is obtained in the whole experimental window.

17.3.1 *Occupancy Patterns*

In (17.16), we have already given the occupancy of a defect after a certain stress and relaxation time under the assumption of an initial empty and finally fully occupied defect. This can be easily generalized as shown in the following.

17.3.1.1 DC Stress

Given that the defect has the occupancy $f(t_0)$ at time t_0, its occupancy after a stress time of duration t_s is

$$f(t_0 + t_s) = f_s + (f(t_0) - f_s)e^{-t_s k_s}, \tag{17.21}$$

while after an additional recovery time t_r one has

$$f(t_0 + t_s + t_r) = f_r + (f(t_0 + t_s) - f_r)e^{-t_r k_r}. \tag{17.22}$$

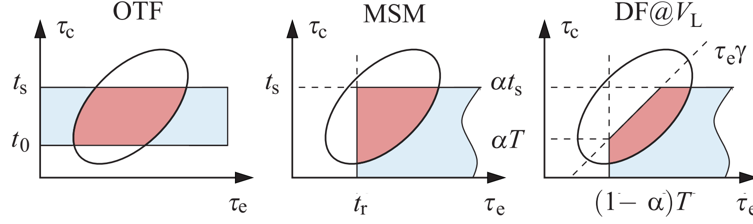

Fig. 17.7 Depending on the measurement scheme, a certain fraction of the CET map can contribute to ΔV_{th}. *Left*: An on-the-fly setup (OTF) misses $\tau_c < t_0$. *Middle*: A measure-stress-measure (MSM) setup misses $\tau_e < t_r$. *Right*: An AC stress results in a trapezoidal region

The occupancy after infinitely long stress would be f_s, while after an infinitely long recovery we have f_r. Both occupancies follow directly from the bias- and temperature-dependent rates

$$f_s = k_{12}/(k_{12}+k_{21})|_{\text{stress}}, \qquad k_s = k_{12}+k_{21}|_{\text{stress}}, \tag{17.23}$$

$$f_r = k_{12}/(k_{12}+k_{21})|_{\text{relax}}, \qquad k_r = k_{12}+k_{21}|_{\text{relax}}. \tag{17.24}$$

As initial condition we assume that all defects have their equilibrium occupancy at the off-voltage, $f(t_0=0) = f_r$ and measure only the deviation from f_r, which reads

$$\Delta f(t_s) = (f_s - f_r)(1 - e^{-t_s k_s}). \tag{17.25}$$

Upon termination of the stress, we have after a recovery time of t_r

$$\Delta f(t_s, t_r) = \Delta f(t_s) e^{-t_r k_r}, \tag{17.26}$$

which is of the same form as (17.16), except for the prefactor $(f_s - f_r)$. This prefactor cannot be extracted from macroscopic data and will be tacitly moved into the CET map g. Note that if the equilibrium occupancies differ from 0 or 1, this means that the defect produces RTN.

As before, if we assume now a collection of defects with distributed k_s and k_r, (17.25) and (17.26) can be used to calculate the occupancy of each defect after a stress time t_s and recovery time t_r: from (17.25) it follows that all defects with $k_s < 1/t_s$ will remain unoccupied, while (17.26) says that all defects which were occupied during stress will already be unoccupied again if $k_r > 1/t_r$. These two conditions describe a rectangular area in the CET map, shown in Fig. 17.7.

17.3.1.2 AC Stress

The above procedure can be easily generalized to digital on-off (AC) stress [36, 38, 79], with duty factor α and period T. After the first cycle we have the occupancies

$$s_1 = f_s + (f_r - f_s)s \tag{17.27}$$

$$r_1 = f_r + (s_1 - f_r)r \tag{17.28}$$

with $s = \exp(-\alpha T k_\mathrm{s})$ and $r = \exp(-(1-\alpha)T k_\mathrm{r})$. Continuing this scheme recursively for n cycles, we obtain a simple geometric series in $B = sr$, which eventually gives

$$\Delta s_n = (f_\mathrm{s} - f_\mathrm{r})(1 - B^n)\frac{1-s}{1-B}, \tag{17.29}$$

$$\Delta r_n = \Delta s_n r. \tag{17.30}$$

After a certain stress time t_s, the cycle number is obtained via $n = \lceil t_\mathrm{s}/T \rceil$. Since n will be a large integer number in practical cases, we consider it a continuous variable to simplify the notation, $n \approx t_\mathrm{s}/T$. The dominant term in (17.29) is B^n, or

$$B^n = (sr)^n = \mathrm{e}^{-nT(\alpha k_\mathrm{s} + (1-\alpha)k_\mathrm{r})} \doteq \mathrm{e}^{-n\alpha T k_\mathrm{AC}} \tag{17.31}$$

with $k_\mathrm{AC} \doteq k_\mathrm{s} + k_\mathrm{r}/\gamma$ and $\gamma = \alpha/(1-\alpha)$. Thus, we have

$$\Delta s_n = (f_\mathrm{s} - f_\mathrm{r})(1 - \mathrm{e}^{-\alpha t_\mathrm{s} k_\mathrm{AC}})\frac{1 - \mathrm{e}^{-\alpha T k_\mathrm{s}}}{1 - \mathrm{e}^{-\alpha T k_\mathrm{AC}}}. \tag{17.32}$$

Equation (17.32) gives the occupancy of a certain defect with effective rates k_s and k_r after a stress time t_s. The first exponential factor gives a transition from 1 to 0 when $\alpha t_\mathrm{s} \approx 1/k_\mathrm{AC}$, thereby giving the upper bound of the trapezoidal region shown in Fig. 17.7. For small k_s and k_r, the last term can be approximated using $\exp(-x) \approx 1 - x$ as

$$\frac{1 - \mathrm{e}^{-\alpha T k_\mathrm{s}}}{1 - \mathrm{e}^{-\alpha T k_\mathrm{AC}}} \approx \frac{k_\mathrm{s}}{k_\mathrm{s} + k_\mathrm{r}/\gamma}. \tag{17.33}$$

This term results in the diagonal of the trapezoidal region [36]. To see this, take a fixed k_r (or τ_e), for which this term becomes 0 for small k_s (large τ_c) and 1 for large k_s (small τ_c), with the transition occurring roughly at $k_\mathrm{s} = k_\mathrm{r}/\gamma$, or $\tau_\mathrm{c} = \tau_\mathrm{e}\gamma$.

17.3.2 The Capture Time Map

Occasionally, we are not that much interested in the details of recovery, for example when we want to determine the worst-case degradation under constant bias stress. We can then simplify the problem to a certain degree by collapsing the τ_e axis of the full distribution $g(\tau_\mathrm{c}, \tau_\mathrm{e})$. For instance, a typical measure-stress-measure (MSM) setup will require a certain delay t_M with which the degradation can be determined. Thus, in order to calculate the degradation at a certain stress time t_s measured with

a certain measurement delay t_M, we integrate over the τ_e axis starting from t_M until infinity, see Fig. 17.7. This includes the contribution of all defects $\tau_\mathrm{e} > t_\mathrm{M}$ because they have not yet emitted their charge. We therefore define the capture time map as

$$g_\mathrm{c}(\tau_\mathrm{c}, t_\mathrm{M}) = \int_{t_\mathrm{M}}^{\infty} g(\tau_\mathrm{c}, \tau_\mathrm{e})\, \mathrm{d}\tau_\mathrm{e} \tag{17.34}$$

which completely determines ΔV_th as

$$\Delta V_\mathrm{th}(t_\mathrm{s}, t_\mathrm{M}) = \int_0^{t_\mathrm{s}} g_\mathrm{c}(\tau_\mathrm{c}, t_\mathrm{M})\, \mathrm{d}\tau_\mathrm{c} = G_\mathrm{c}(t_\mathrm{s}, t_\mathrm{M}) \tag{17.35}$$

because $G_\mathrm{c}(0, t_\mathrm{M})$ must vanish. In fact, if we chose to normalize $g_\mathrm{c}(\tau_\mathrm{c}, t_\mathrm{M})$, it would be just like the probability density function of ΔV_th while $G(\tau_\mathrm{c})$ would correspond to the cumulative distribution function. However, as we shall see in the sequel, this analogy should not be taken too far, since g and g_c can have a negative sign if non-first-order processes are considered. This is for instance the case when the prediction of the reaction–diffusion model is cast into this formalism. Also, the loss of defects over time may result in negative entries in g. While these more subtle points will not be discussed in the following, they may prove crucial in the near future and are the reason why g is referred to as *map* rather than *distribution*.

In delay-free experiments, which have become known as on-the-fly (OTF) measurements [80, 81], the measurement delay is zero and the capture time map covers the whole τ_e axis. In practice, however, a delay-free experiment requires determination of a reference value for the calculation of ΔV_th. This reference value is determined with a certain delay t_M at the stress voltage, which corresponds to

$$\Delta V_\mathrm{th}^\mathrm{OTF}(t_\mathrm{s}, t_\mathrm{M}) = \int_{t_\mathrm{M}}^{t_\mathrm{s}} g_\mathrm{c}(\tau_\mathrm{c}, 0)\, \mathrm{d}\tau_\mathrm{c}. \tag{17.36}$$

As a result, even OTF measurements do not capture all defects as the lower part of the τ_c axis is missed. The opposite is true for MSM setups which cover the complete τ_c axis but only a part of the τ_e axis. The difference between the two setups is visualized in Fig. 17.7.

Equations (17.35) and (17.36) now provide a simple procedure for the extraction of $g_\mathrm{c}(\tau_\mathrm{c}, t_\mathrm{M})$ from a given $\Delta V_\mathrm{th}(t_\mathrm{s}, t_\mathrm{M})$,

$$g_\mathrm{c}(\tau_\mathrm{c}, t_\mathrm{M}) = \frac{\mathrm{d}\Delta V_\mathrm{th}(\tau_\mathrm{c}, t_\mathrm{M})}{\mathrm{d}\tau_\mathrm{c}} \quad \text{and} \quad g_\mathrm{c}(\tau_\mathrm{c}, 0) = \frac{\mathrm{d}\Delta V_\mathrm{th}^\mathrm{OTF}(\tau_\mathrm{c}, t_\mathrm{M})}{\mathrm{d}\tau_\mathrm{c}}, \tag{17.37}$$

the first including the delay of the MSM measurement while the second being valid for OFT data with $\tau_\mathrm{c} > t_\mathrm{M}$.

17.3.3 The Logarithmic Capture/Emission Time Map

So far we have defined the two-dimensional capture/emission time map as well as its reduced one-dimensional counterpart, the capture time maps. These maps give the density of defects having certain time constants on a *linear* axis. As we shall see in the sequel, it is useful to transform the density onto *logarithmic* axes. Such a transformation is inspired by the typically observed power-law degradation behavior, which corresponds to a straight line on a double logarithmic plot, as well as by the typically observed logarithmic recovery. In particular, the latter implies that about the same amount of charge is lost per decade in time, see Fig. 17.6.

We start by introducing

$$\theta_c = \log(\tau_c/\tau_0) \qquad \text{and} \qquad \theta_e = \log(\tau_e/\tau_0)\,, \tag{17.38}$$

with a suitably chosen τ_0. For the time being, τ_0 serves the purpose of a normalization constant, while θ is merely the logarithm of a normalized time constant. However, as physical models for the time constants can usually be cast into the form $\tau = \tau_0 \exp(\theta)$, this already implies the basic structure of the physical model, as hinted at in (17.1).

Instead of integrating over τ, we rewrite the integration of g as an integration over θ

$$\begin{aligned} \Delta V_{\text{th}}(t_s,t_r) &= \int_0^{t_s} \mathrm{d}\tau_c \int_{t_r}^{\infty} \mathrm{d}\tau_e\; g(\tau_c,\tau_e) \\ &= \int_{-\infty}^{\log(t_s/\tau_0)} \mathrm{d}\theta_c \int_{\log(t_r/\tau_0)}^{\infty} \mathrm{d}\theta_e\; g(\tau_0 e^{\theta_c}, \tau_0 e^{\theta_e})\, \tau_0 e^{\theta_c}\, \tau_0 e^{\theta_e}. \end{aligned} \tag{17.39}$$

With $\theta_s = \log(t_s/\tau_0)$, $\theta_r = \log(t_r/\tau_0)$, and

$$\tilde{g}(\theta_c,\theta_e) = g(\tau_0 e^{\theta_c}, \tau_0 e^{\theta_e})\, \tau_0 e^{\theta_c}\, \tau_0 e^{\theta_e} \tag{17.40}$$

we can finally write

$$\Delta V_{\text{th}}(t_s,t_r) = \int_{-\infty}^{\theta_s} \mathrm{d}\theta_c \int_{\theta_r}^{\infty} \mathrm{d}\theta_e\; \tilde{g}(\theta_c,\theta_e) = \tilde{G}(\theta_s,\infty) - \tilde{G}(\theta_s,\theta_r). \tag{17.41}$$

Equation (17.40) handles the transformation from the linear to the logarithmic scale, with $\tilde{g}(\theta_c,\theta_e)$ as the logarithmic CET map. Conversely, we have the inverse transformation

$$g(\tau_c,\tau_e) = \frac{\tilde{g}(\log(\tau_c/\tau_0),\log(\tau_e/\tau_0))}{\tau_c\tau_e}. \tag{17.42}$$

Similarly, the transformation rules for the linear and logarithmic capture time maps are

$$\tilde{g}_\mathrm{c}(\theta_\mathrm{c}) = g_\mathrm{c}(\tau_0 \mathrm{e}^{\theta_\mathrm{c}})\,\tau_0 \mathrm{e}^{\theta_\mathrm{c}} \qquad \text{and} \qquad g_\mathrm{c}(\tau_\mathrm{c}) = \frac{\tilde{g}_\mathrm{c}(\log(\tau_\mathrm{c}/\tau_0))}{\tau_\mathrm{c}}. \tag{17.43}$$

With the logarithmic capture time map, ΔV_th can be obtained as

$$\Delta V_\mathrm{th}(t_\mathrm{s}) = \int_{-\infty}^{\theta_\mathrm{s}} \tilde{g}_\mathrm{c}(\theta_\mathrm{c})\,\mathrm{d}\theta_\mathrm{c} = \tilde{G}_\mathrm{c}(\theta_\mathrm{s}). \tag{17.44}$$

17.3.4 Properties of the Capture Time Map

So far we have derived theoretical relations which describe the connections between the various maps and the experimentally observed degradation. No assumptions on their functional forms have been made. Naturally, any experimentally observed degradation and recovery behavior will require a unique CET map.

For simplicity, we start with the capture time map, which can be calculated from a known $\Delta V_\mathrm{th}(t_\mathrm{s})$. Experimentally, two functional forms of $\Delta V_\mathrm{th}(t_\mathrm{s})$ are of importance, namely the logarithmic degradation, $\log(t_\mathrm{s}/t_0)$, particularly for short-time data [82, 83], and the power-law t_s^n [50, 68]. The capture time maps required to produce such a time behavior will be derived in the following.

17.3.4.1 Logarithmic Time Behavior

Assume that the experimentally observed degradation follows a logarithm in time,

$$\Delta V_\mathrm{th}(t_\mathrm{s}) = A\log(t_\mathrm{s}/t_0) \tag{17.45}$$

starting from a certain time $t_\mathrm{s} \geq t_0$ as sketched in Fig. 17.8. In NBTI data, the point t_0 is typically outside the measurement window [83]. According to (17.37) we obtain

$$g_\mathrm{c}(\tau_\mathrm{c}) = \frac{\mathrm{d}\Delta V_\mathrm{th}(\tau_\mathrm{c})}{\mathrm{d}\tau_\mathrm{c}} = \frac{A}{\tau_\mathrm{c}}, \tag{17.46}$$

which corresponds to the p.d.f. of a log-uniform distribution. This is easier to see when g_c is transformed on the logarithmic θ_c axis using (17.43)

$$\tilde{g}_\mathrm{c}(\theta_\mathrm{c}) = g_\mathrm{c}(\tau_0 \mathrm{e}^{\theta_\mathrm{c}})\,\tau_0 \mathrm{e}^{\theta_\mathrm{c}} = A \tag{17.47}$$

for $\theta_\mathrm{c} \geq \log(t_0/\tau_0)$ and shown in Fig. 17.8.

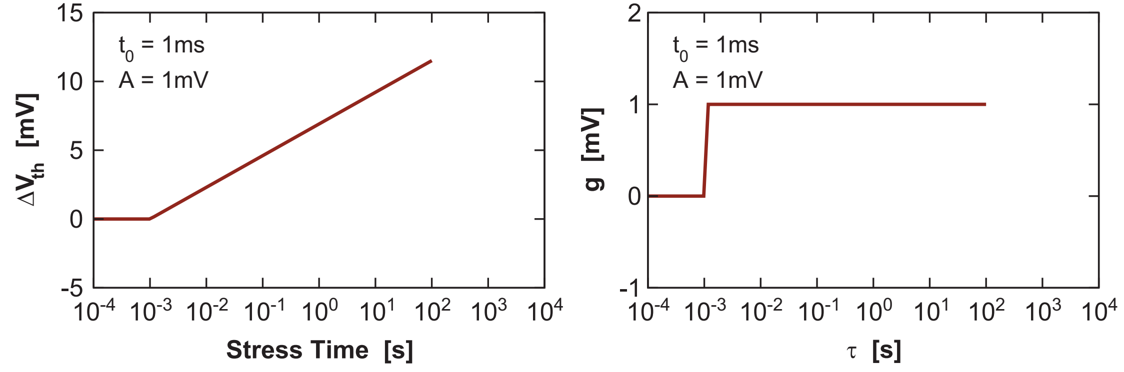

Fig. 17.8 *Left*: Logarithmic time evolution of ΔV_{th}. *Right*: The corresponding logarithmic capture time map

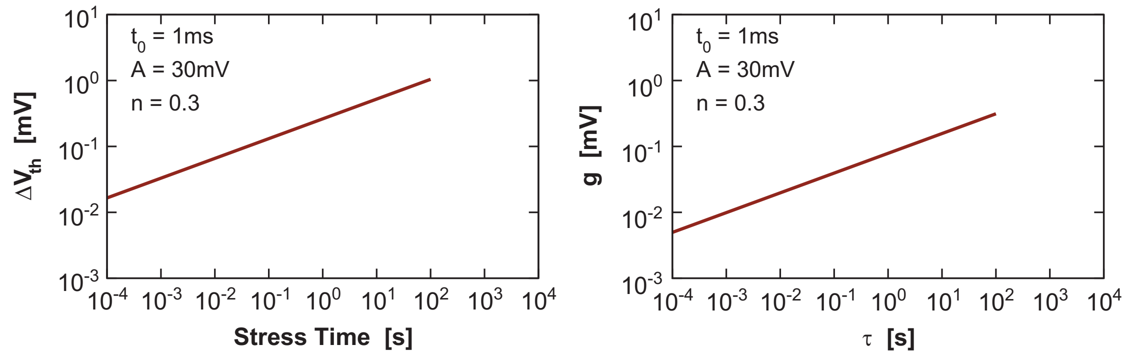

Fig. 17.9 *Left*: Power-law time evolution of ΔV_{th}. *Right*: The corresponding logarithmic capture time map

17.3.4.2 Power-Law Time Behavior

Assume now that the degradation follows a power-law in time,

$$\Delta V_{\text{th}}(t_{\text{s}}) = A\left(\frac{t_{\text{s}}}{t_0}\right)^n \tag{17.48}$$

as shown in Fig. 17.9. By making use of (17.37) as before, we obtain

$$g(\tau_{\text{c}}) = \frac{\text{d}\Delta V_{\text{th}}(\tau_{\text{c}})}{\text{d}\tau_{\text{c}}} = A\frac{n}{t_0^n}\frac{1}{\tau_{\text{c}}^{1-n}} \tag{17.49}$$

for $t_{\text{s}} \geq t_0$. On the logarithmic axis we have

$$\tilde{g}(\theta_{\text{c}}) = An\left(\frac{\tau_0}{t_0}\right)^n \text{e}^{n\theta_{\text{c}}}. \tag{17.50}$$

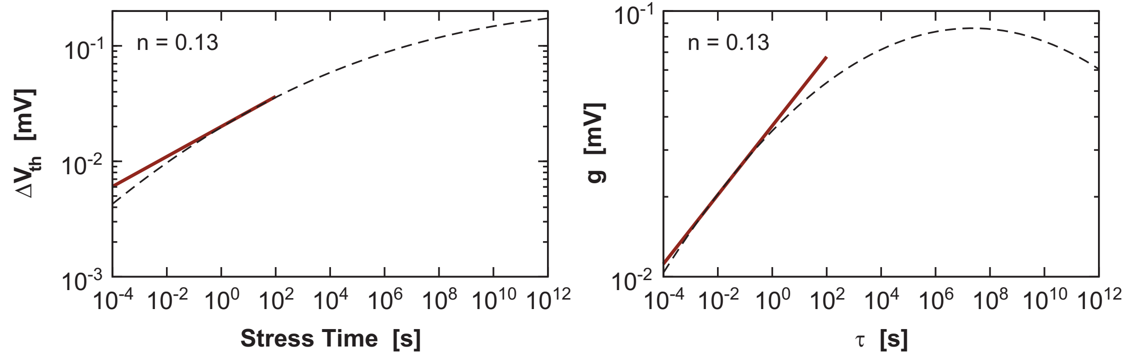

Fig. 17.10 *Left*: Power-law time evolution (*solid line*) as a short-time property of a Gaussian distribution (*dashed line*) ΔV_{th}. *Right*: The corresponding logarithmic capture time map

This can be written as a function of $\tau_c(\theta_c)$ as

$$\tilde{g}(\tau_c) = A\frac{n}{t_0^n}\tau_c^n. \tag{17.51}$$

In words, a power-law degradation in time requires a logarithmic density which increases following a power-law in τ_c with the same exponent n, see Fig. 17.9.

17.3.4.3 Discussion

In summary, the two cases of the logarithmic and power-law time-dependence will result from the following distributions

$$\begin{aligned} &\text{Logarithmic:} && g_c(\tau_c) \sim 1/\tau_c && \tilde{g}_c(\theta_c) \sim \text{const.} \\ &\text{Power-Law:} && g_c(\tau_c) \sim 1/\tau_c^{1-n} && \tilde{g}_c(\theta_c) \sim e^{n\theta_c} = \tau_c^n \end{aligned}$$

The power-law exponent typically observed is rather small, say $n = 0.15$, which results in $g(\tau_c) \sim 1/\tau_c^{0.85}$. This is reminiscent to the problem of $1/f$ noise [84]: theoretically, a uniform distribution in θ results in $1/f$ noise. Experimentally, however, one often sees something more like $1/f^\alpha$, with exponents close to unity, which then would correspond to a "power-law" distribution.

The fundamental question that springs to mind is how these distributions will behave for larger τ_c. For example, a perfect power-law requires an indefinitely increasing $\tilde{g}_c$, which is clearly not a sensible option. It is thus important to realize that $\tilde{g}_c$ measured over a limited time window can only provide some local snapshot of a more general distribution, which eventually has to saturate and fall off. A natural example for such a distribution would be a Gaussian distribution on a logarithmic scale, see Fig. 17.10. As will be discussed in more detail below, a wide Gaussian distribution will produce a power-law in time over many decades, albeit with a slight curvature. Indeed, while such a deviation from the power-law can also be attributed to the influence of the measurement delay [68, 85, 86], a curvature can be clearly observed also in long-term OTF data [49, 87–89].

17.3.5 Physical Origin of the Capture Time Map

As discussed above, one cannot expect the power-law degradation to continue indefinitely in time. The most obvious explanation would be that the (partial) distribution $e^{n\theta}$ is the tail of a more realistic distribution that, after having reached its peak, eventually levels off with increasing θ.

17.3.5.1 Tail of a Gaussian Distribution

The natural choice for such a distribution would be the Gaussian distribution of θ as $\tilde{g}_c(\theta_c) = \Delta V_{th}^{max} f(\theta_c)$ with

$$f_g(\theta) = \frac{1}{\sqrt{2\pi}\sigma} \exp\Big(-\frac{(\theta-\mu)^2}{2\sigma^2}\Big) \tag{17.52}$$

Taking the Taylor expansion of $\log(f)$ at some $\theta_0 < \mu$ we have

$$f_g(\theta) \approx f_g(\theta_0) e^{-n\theta_0} e^{n\theta} = \frac{1}{\sqrt{2\pi}\sigma} \exp\Big(\frac{\theta_0^2 - \mu^2}{2\sigma^2}\Big) e^{n\theta} \tag{17.53}$$

with the power-law exponent

$$n = \Big[\frac{1}{f_g(\theta)} \frac{df_g(\theta)}{d\theta}\Big]_{\theta=\theta_0} = \frac{\mu - \theta_0}{\sigma^2}. \tag{17.54}$$

Recall that $\theta_0 < \mu$ was assumed, so $n > 0$ as it should be.

We have already shown that for a certain region around θ_0 a Gaussian distribution results in a power-law in time. The full time evolution including the curvature and eventual saturation can be obtained from $\tilde{g}_c(\theta_c) = \Delta V_{th}^{max} f_g(\theta_c)$ as

$$\Delta V_{th}(t_s) = \frac{\Delta V_{th}^{max}}{2} \operatorname{erfc}\Big(\frac{\mu - \log(t_s/\tau_0)}{\sqrt{2}\sigma}\Big). \tag{17.55}$$

17.3.5.2 Tail of a Logistic Distribution

Rather than using a Gaussian distribution, which results in awkward error functions when integrated, the use of the logistic distribution

$$f_l(\theta) = \frac{1}{s} \frac{\exp\Big(\frac{\mu-\theta}{s}\Big)}{\Big(1+\exp\Big(\frac{\mu-\theta}{s}\Big)\Big)^2} \tag{17.56}$$

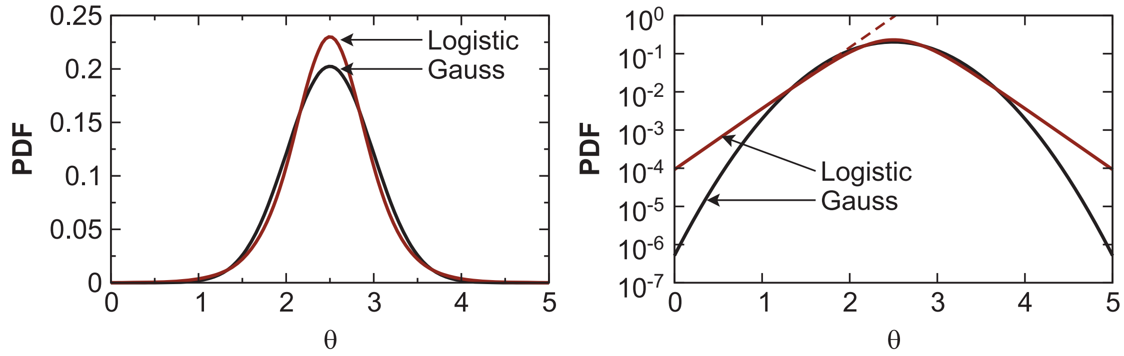

Fig. 17.11 *Left*: On a linear scale, the logistic distribution appears to be very similar to a Gaussian distribution. For this comparison the same mean and standard deviation ($\mu = 2.5$ and $\sigma = 0.5$) were chosen. A slight increase in the standard deviation of the logistic distribution to 0.56 would further increase the visual similarity (not shown). *Right*: On a logarithmic y-axis, one can see that the tails of the logistic distribution are linear in θ while for the Gaussian distribution they depend quadratically on θ. As a consequence, the Gaussian distribution always has a curvature on a log-lin plot

has been suggested [90], with mean μ and parameter s. The standard deviation of the logistic distribution is $\sigma = s\pi/\sqrt{3}$. When plotted using a linear y-axis, the logistic distribution appears like a Gaussian hump, see Fig. 17.11. In contrast to the Gaussian distribution, however, it can be easily integrated and results in the Fermi function

$$F_1(\theta) = \frac{1}{1 + \exp\left(\frac{\mu - \theta}{s}\right)}. \tag{17.57}$$

Because of this property, the logistic distribution is sometimes called Fermi-derivative distribution [90]. The most tempting choice to explain the power-law is to assume $\theta \ll \mu$ [90], for which the logistic distribution can be approximated by

$$f_1(\theta) \approx \frac{1}{s} \exp\left(\frac{\theta - \mu}{s}\right), \tag{17.58}$$

which would perfectly correspond to the density $\tilde{g}(\theta)$ required for a power-law in time. Then, the power-law exponent would be given by $n = 1/s = \pi/\sqrt{3}\sigma$. Albeit tempting, we will see later that this is an unfortunate choice, since one may be lead to the wrong conclusion that the logistic distribution is incompatible with experimental data. To obtain the "correct" results, we expand the distribution in a more general fashion as in the Gaussian case, which leads to

$$n = \frac{1}{s} \frac{\exp\left(\frac{\mu - \theta}{s}\right) + 1}{\exp\left(\frac{\mu - \theta}{s}\right) - 1}. \tag{17.59}$$

The above will only give the conventional $n \approx 1/s$ for θ far below the mean, that is, $\theta \ll \mu$. However, as will be shown in the following sections, it is only this more general form of the power-law exponent which is consistent with experimental data. In this general case, the time evolution of ΔV_{th} resulting from a logistic distribution is

$$\Delta V_{\mathrm{th}}(t_{\mathrm{s}}) = \frac{\Delta V_{\mathrm{th}}^{\mathrm{max}}}{1 + \mathrm{e}^{\mu/s}\left(\frac{\tau_0}{t_{\mathrm{s}}}\right)^{1/s}}. \tag{17.60}$$

17.3.6 Simple Thermal Activation Model

So far we have established that an exponential density $g(\theta_{\mathrm{c}}) = \mathrm{e}^{n\theta_{\mathrm{c}}}$ is required for a power-law in time. Also, this exponential density can be justified as the tail of either a Gaussian or a logistic distribution. What remains to be seen is the *physical meaning* of the relation $\tau_{\mathrm{c}} = \tau_0 \mathrm{e}^{\theta_{\mathrm{c}}}$. In other words, what physical model would give time constants of the form $\tau_{\mathrm{c}} = \tau_0 \mathrm{e}^{\theta_{\mathrm{c}}}$?

As already hinted at in the discussion on the physical models around (17.1), the most obvious choice that springs to mind is the Arrhenius law, $\tau_{\mathrm{c}} = \tau_0 \mathrm{e}^{\beta \mathscr{E}_{\mathrm{c}}}$. In that case, the physical meaning of θ would be given by the activation energy of the process,

$$\mathscr{E}_{\mathrm{c}} = \theta_{\mathrm{c}}/\beta. \tag{17.61}$$

Also, rather than assuming that θ_{c} is distributed according to a certain distribution, it appears more sensible to assume that it is the activation energy itself which is distributed. The difference between these two assumptions is fundamental, as in the latter case the distribution of θ_{c} will depend on temperature while in the former case it will not. Whichever option is correct can then be easily determined by verifying the “built-in” temperature dependence of the model with experimental data.

For the simple distributions discussed here, we only need to be concerned about the mean $\bar{\mathscr{E}}_{\mathrm{c}}$ and the standard deviation σ_{c} of the activation energy. It follows from basic statistical laws that the according moments of the transformed distribution θ are $\mu = \bar{\mathscr{E}}_{\mathrm{c}}/\mathrm{k_B}T$ and $\sigma = \sigma_{\mathrm{c}}/\mathrm{k_B}T$.

The fundamental question to answer here is whether these distributions are compatible with the experimentally observed temperature-independent power law exponents. At a first glance, this is anything but obvious and has led to claims that such distributions are incompatible with data. We start by writing the time evolution of a Gaussian distribution

$$\Delta V_{\mathrm{th}}(t_{\mathrm{s}}) = \frac{\Delta V_{\mathrm{th}}^{\mathrm{max}}}{2} \mathrm{erfc}\left(\frac{\bar{\mathscr{E}}_{\mathrm{c}} - \mathrm{k_B}T \log(t_{\mathrm{s}}/\tau_0)}{\sqrt{2}\sigma_{\mathrm{c}}}\right), \tag{17.62}$$

which can be approximated by a power law around a certain measurement window given by $\tau_0 \exp(\theta_0)$. The slope of this power law is obtained from (17.54) and (17.61) as

$$n = \frac{\bar{\mathscr{E}}_c/k_B T - \theta_0}{(\sigma_c/k_B T)^2} \tag{17.63}$$

and apparently depends on temperature. However, the important point to see here is that the measurement point θ_0 is determined by the experimental window and is therefore not temperature-dependent. If θ_0 were much smaller than $\bar{\mathscr{E}}_c/k_B T$, n would be clearly temperature-dependent. If, however, θ_0 is say about half of $\bar{\mathscr{E}}_c/k_B T$, the data will appear temperature-independent in a certain window around θ_0.

Let us now try to work out under what circumstances (17.63) can give a temperature-independent n and whether such a scenario makes physical sense. We start by assuming that we measure the degradation at two different temperatures, say T_1 and T_2. As we have to be consistent with the experimental observation that n is temperature-independent, we require n to have the same value at both temperatures,

$$\frac{\bar{\mathscr{E}}_c/k_B T_1 - \theta_0}{(\sigma_c/k_B T_1)^2} = \frac{\bar{\mathscr{E}}_c/k_B T_2 - \theta_0}{(\sigma_c/k_B T_2)^2}. \tag{17.64}$$

From this we see that a given measurement range around θ_0 determines the required mean activation energy $\bar{\mathscr{E}}_c$

$$\bar{\mathscr{E}}_c = \theta_0 k_B (T_1 + T_2). \tag{17.65}$$

Then, in order to give a certain temperature-independent power law slope n, for instance $n = 1/6$, we can calculate the required σ_c from

$$n = \frac{\bar{\mathscr{E}}_c/k_B T_1 - \theta_0}{(\sigma_c/k_B T_1)^2} \tag{17.66}$$

as

$$\sigma_c^2 = \theta_0 \frac{{k_B}^2}{n} T_1 T_2. \tag{17.67}$$

Long-term power-law exponents are usually determined in the range 100 s to 1 ks. This rather firmly sets the value of θ_0, for instance to $\theta_0 \approx \log(250\,\mathrm{s}/\tau_0)$. When we now assume $T_1 = 100\,^\circ\mathrm{C}$ and $T_2 = 200\,^\circ\mathrm{C}$, we obtain from (17.65) a mean activation energy of $\bar{\mathscr{E}}_c = 2.25\,\mathrm{eV}$. Finally, with $n = 1/6$ we obtain from (17.67) a standard deviation of $\sigma_c = 0.5\,\mathrm{eV}$. Both $\bar{\mathscr{E}}_c$ and σ_c appear sensible parameters of a distribution of activation energies in an amorphous oxide. The conditions on the parameters can be relaxed when we merely require a roughly temperature-independent n.

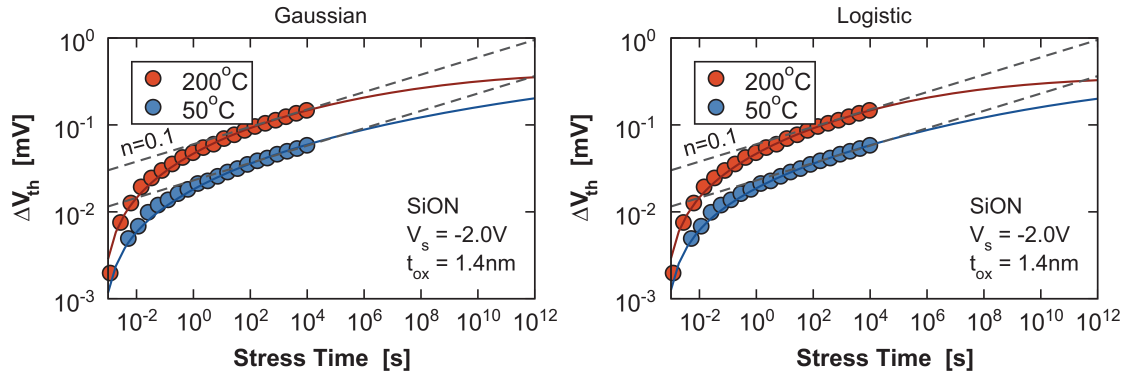

Fig. 17.12 OTF measurement on a 1.4 nm PNO device at two temperatures fitted by Gaussian (*left*) and a logistic (*right*) distribution of activation energies. Both fits are virtually indistinguishable in the measurement window, reproduce the temperature-independent power-law, but differ slightly in their long term prediction. The reference value of the measurement was obtained at $t_{\mathrm{M}} = 1\,\mathrm{ms}$, which is emulated in the fits by subtracting $\Delta V_{\mathrm{th}}(t_{\mathrm{M}})$ and visible as a rapid increase in ΔV_{th} for $t_{\mathrm{s}} > t_{\mathrm{M}}$

Similar conclusions can be drawn for the logistic distribution. However, in the approximation where the logistic distribution is expanded far away from the maximum, as is usually done in literature, the resulting power-law exponent n will be linearly temperature-dependent, $n = \mathrm{k_B}T/s$. As stated above, this is contrary to experimental observations. However, this must not be mistaken as a failure of the logistic distribution itself, but rather as a consequence of an unfavorable approximation. Suitable approximations can only be obtained when the distribution is expanded somewhere closer to the mean rather than in the tail, quite similar to the Gaussian case, see Fig. 17.12. While both fits have virtually the same quality inside the measurement window, they behave slightly different at longer times. Since the Gaussian distribution appears a more natural choice for the distribution of activation energies, it will be preferred in the following. Another reason is that the mathematical advantage of the logistic distribution cannot be exploited for the two-dimensional capture/emission time maps.

17.4 The Analytic CET Map

In the following we try to generalize our previous observations to derive an empirical analytical model for the CET map. The model is based on the following assumptions:

- The CET map will consist of two distributions, one describing the recoverable component R, the other the more permanent contribution P. Lacking firm evidence to the contrary, we take the simplest route and assume for the time being that these components are independent.

- We have also seen before that many experimental features like the power-law dependence can be captured by a Gaussian distribution for τ_c, which appears a natural choice.
- We assume that the effective activation energies are distributed, which results in a particular "built-in" temperature dependence of the model. The bias-dependence, on the other hand, must be added by making some parameters of the model bias-dependent [37].
- Visual inspection of the numerically extracted CET map in Fig. 17.6 shows that the emission times become larger with increasing capture times, implying a correlation between the two. The simplest way to express this mathematically is to write the activation energy of τ_e in the form $\mathscr{E}_e = \mathscr{E}_c + \Delta\mathscr{E}_e$, where $\Delta\mathscr{E}_e$ describes an uncorrelated part of $\mathscr{E}_e$. Again, we assume that $\Delta\mathscr{E}_e$ follows a Gaussian distribution.

In the following we assume that both oxide traps and interface traps can be written in the form (17.14)

$$\tau_c = \tau_0 e^{\beta \mathscr{E}_c} \quad \text{and} \quad \tau_e = \tau_c e^{\beta \Delta \mathscr{E}_e}. \tag{17.68}$$

Again, the only justification of this assumption will be the agreement with experimental data demonstrated later on. In order to proceed, we need to know the joint probability density function $g(\tau_c, \tau_e)$ which characterizes the distribution of both time constants. In general, all three quantities in the above, τ_0, $\mathscr{E}_c$, $\Delta\mathscr{E}_e$ will be distributed. RTN experiments [65] show no correlation between the depth of the defect into the oxide, which should essentially determine the distribution of τ_0 via the WKB factor, and τ_e and τ_c. Also, the time constants will depend much weaker on a distribution of τ_0 compared to a distribution of the energies. We therefore assume that the energy distribution to be the dominant contribution. As such, we need to find a model for the joint distribution $g(\mathscr{E}_c, \mathscr{E}_e)$, with $\mathscr{E}_e = \mathscr{E}_c + \Delta\mathscr{E}_e$. This distribution is easy to construct via the conditional "probability" $g(\mathscr{E}_e|\mathscr{E}_c)$ and noting that

$$g(\mathscr{E}_c, \mathscr{E}_e) = g(\mathscr{E}_e|\mathscr{E}_c)\, g(\mathscr{E}_c). \tag{17.69}$$

The conditional probability $g(\mathscr{E}_e|\mathscr{E}_c)$ is the probability of obtaining a certain value of $\mathscr{E}_e$ for a fixed $\mathscr{E}_c$. Since we assume $\Delta\mathscr{E}_e$ to be Gaussian distributed with standard deviation $\sigma_{\Delta e}$, we have

$$g(\mathscr{E}_e|\mathscr{E}_c) = \frac{1}{\sigma_{\Delta e}} \phi\left(\frac{\mathscr{E}_e - (\mathscr{E}_c + \mu_{\Delta e})}{\sigma_{\Delta e}}\right). \tag{17.70}$$

Thus, in total we obtain

$$g(\mathscr{E}_c, \mathscr{E}_e) = \frac{1}{\sigma_c \sigma_{\Delta e}} \phi\left(\frac{\mathscr{E}_c - \mu_c}{\sigma_c}\right) \phi\left(\frac{\mathscr{E}_e - (\mathscr{E}_c + \mu_{\Delta e})}{\sigma_{\Delta e}}\right) \tag{17.71}$$

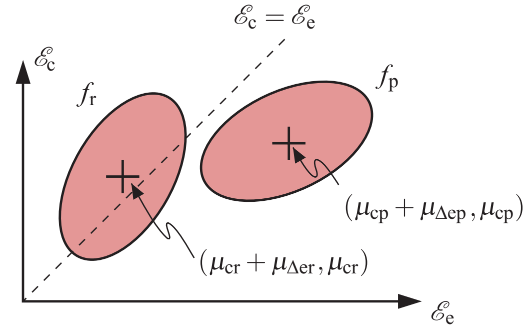

Fig. 17.13 The CET map is modeled in the activation-energy-space using two bivariate Gaussian distributions, one for the recoverable component, f_r, and one for the more permanent component, f_p

which is a bivariate Gaussian distribution. We will use such a bivariate Gaussian distribution to describe both the recoverable and the "permanent" part of the degradation as sketched in Fig. 17.13. The following properties of the above joint distribution are worth mentioning:

- The marginal distribution for $\mathcal{E}_e$, which is obtained by integrating $g(\mathcal{E}_c, \mathcal{E}_e)$ over $\mathcal{E}_c$, is a Gaussian with $\mu_e = \mu_c + \mu_{\Delta e}$ and $\sigma_e^2 = \sigma_c^2 + \sigma_{\Delta e}^2$.
- The correlation coefficient is $\rho = \sigma_c / \sigma_e$. Note that this correlation coefficient is a consequence of our Ansatz for $\mathcal{E}_e$ and thus not directly a parameter of the model.

By introducing the normalized variates

$$x(\mathcal{E}_e) = \frac{\mathcal{E}_e - (\mu_c + \mu_{\Delta e})}{\sigma_e} \quad \text{and} \quad y(\mathcal{E}_c) = \frac{\mathcal{E}_c - \mu_c}{\sigma_c}, \tag{17.72}$$

the bivariate Gaussian distribution (17.71) can be written in standard form

$$f(x, y, \rho) = \frac{\phi(y)}{\sqrt{1-\rho^2}} \phi\left(\frac{x - \rho y}{\sqrt{1-\rho^2}}\right). \tag{17.73}$$

In order to calculate the response to DC stress, we need the sum over all defects with $\tau_c < t_s$ and $\tau_e > t_r$, which corresponds to all defects being charged up to t_s and not yet discharged at t_r. By transforming t_s and t_r to their corresponding energies and then into our normalized (x, y) space as $a = x(\log(t_r/\tau_0)/\beta)$ and $b = y(\log(t_s/\tau_0)/\beta)$, the fraction of all defects contributing is given by the integral

$$\begin{aligned} F(a, b, \rho) &= \int_{-\infty}^{b} \mathrm{d}y \int_{a}^{\infty} \mathrm{d}x f(x, y, \rho) = \int_{-\infty}^{b} \mathrm{d}y\, \phi(y) \int_{a}^{\infty} \mathrm{d}x\, \phi\left(\frac{x - \rho y}{\sqrt{1-\rho^2}}\right) \\ &= \int_{-\infty}^{b} \phi(y) Q\left(\frac{a - \rho y}{\sqrt{1-\rho^2}}\right) \mathrm{d}y \end{aligned} \tag{17.74}$$

with the standard integral of the Gaussian distribution

$$Q(x) = \int_{x}^{\infty} \phi(x)\, \mathrm{d}t = \tfrac{1}{2}\left(1 - \mathrm{erf}\left(\frac{x}{\sqrt{2}}\right)\right) = \tfrac{1}{2}\,\mathrm{erfc}\left(\frac{x}{\sqrt{2}}\right). \tag{17.75}$$

Unfortunately, the integrand of $F(a,b,\rho)$ consists of a Gaussian function multiplied by an error function, which cannot be integrated in closed form. In fact, the calculation of bivariate normal integral poses a standard problem in statistics and numerous solutions to the problem have been proposed over the last decades [91–93]. However, most of these approximations are too crude for our purpose, since our expression needs to capture the integral over a wide range of times and temperatures. A slightly more involved yet simple approach has been suggested recently [94], which is based on approximating $\mathrm{erf}(x)$ in $Q(x)$ as

$$\mathrm{erf}(x) \approx 1 - \mathrm{e}^{-c_1 x - c_2 x^2} \tag{17.76}$$

for $x > 0$ with two fitting parameters c_1 and c_2. The values for $x < 0$ are obtained from $\mathrm{erf}(-x) = -\mathrm{erf}(x)$. A least squares fit in the interval $0 \leq x \leq 3$ gives $c_1 = 1.0950$ and $c_2 = 0.756508$ and a relative error smaller than 0.2% for $x > 0.34$ and smaller than 3% for $0 \leq x \leq 0.34$. The beauty of this approximation is a consequence of the fact that the Gaussian distribution when multiplied by an exponential of a second-order polynomial can be rearranged into a shifted and scaled distribution which can then be integrated and expressed as combinations of normal integrals

$$\Phi(x) = \int_{-\infty}^{x} \phi(x)\,\mathrm{d}t = \tfrac{1}{2}\left(1 + \mathrm{erf}\left(\frac{x}{\sqrt{2}}\right)\right) = \tfrac{1}{2}\,\mathrm{erfc}\left(-\frac{x}{\sqrt{2}}\right). \tag{17.77}$$

A slight price to pay comes from the piecewise integration for $x \leq 0$ and $x > 0$, which corresponds to $a \leq \rho b$ and $a > \rho b$. After some tedious but straightforward manipulations one obtains the slightly daunting but highly accurate expressions

$$\begin{aligned} F(a,b) = {} & \Phi(b) - \Phi\left(\frac{a}{\rho}\right) + \frac{1}{2r_2}\exp\left(\frac{r_1^2 - 2a^2 C_2}{2r_2^2}\right) \\ & \times \left\{ \exp\left(-a\frac{C_1}{r_2^2}\right)\Phi\left(\frac{a/\rho - r_1}{r_2}\right) \right. \\ & \left. + \exp\left(a\frac{C_1}{r_2^2}\right)\left[\Phi\left(\frac{a/\rho + r_1}{r_2}\right) - \Phi\left(\frac{b + r_1 - 2C_2\rho(a - b\rho)}{r_2}\right)\right]\right\} \end{aligned} \tag{17.78}$$

valid for shorter recovery times ($a \leq \rho b$), while for longer recovery times ($a > \rho b$) we have

$$F(a,b) = \frac{1}{2r_2}\exp\left(\frac{r_1^2 - 2a(C_1 + aC_2)}{2r_2^2}\right)\Phi\left(\frac{b - r_1 - 2C_2\rho(a - b\rho)}{r_2}\right)$$

with

$$C_1 = c_1\eta, \quad C_2 = c_2\eta^2, \quad \eta = 1/\sqrt{2(1-\rho^2)}, \tag{17.79}$$

$$r_1 = c_1\rho\eta, \quad r_2^2 = 1 + 2c_2(\rho\eta)^2. \tag{17.80}$$

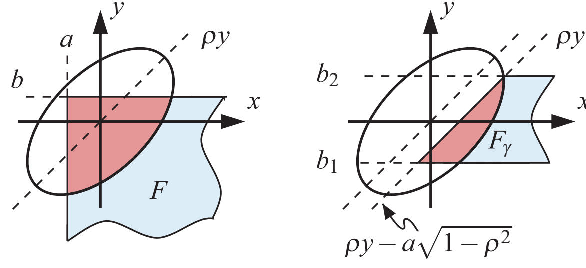

Fig. 17.14 The auxiliary integrals F and F_γ used to calculate the degradation after DC and AC stress

A slightly less accurate but more compact version is obtained by setting $c_1 = \sqrt{3}$ and $c_2 = 0$. By introducing $c = \sqrt{3}\eta$ we then obtain for $a \leq \rho b$

$$F(a,b) = \Phi(b) - \Phi\left(\frac{a}{\rho}\right) + \tfrac{1}{2}\mathrm{e}^{c^2\rho^2/2} \times \left\{\mathrm{e}^{-ca}\Phi\left(\frac{a}{\rho} - c\rho\right) + \mathrm{e}^{ca}\left[\Phi\left(\frac{a}{\rho} + c\rho\right) - \Phi(b + c\rho)\right]\right\}, \tag{17.81}$$

while for $a > \rho b$ we have

$$F(a,b) = \frac{1}{2}\mathrm{e}^{c^2\rho^2/2}\mathrm{e}^{-ca}\Phi(b - c\rho). \tag{17.82}$$

With the above we can write ΔV_{th} after a DC stress of duration t_s and after a recovery time t_r as (see Fig. 17.7)

$$\Delta V_{\mathrm{th}}(t_\mathrm{r}, t_\mathrm{s}) = A_\mathrm{r} G_\mathrm{r}(t_\mathrm{r}, t_\mathrm{s}) + A_\mathrm{p} G_\mathrm{p}(t_\mathrm{r}, t_\mathrm{s}) \tag{17.83}$$

with the auxiliary functions describing the permanent and recoverable peaks

$$G_\mathrm{r}(t_\mathrm{r}, t_\mathrm{s}) = F\left(\frac{\mathrm{k_B}T\log(t_\mathrm{r}/\tau_{0\mathrm{r}}) - \mu_{\Delta\mathrm{er}} - \mu_\mathrm{cr}}{\sigma_\mathrm{er}}, \frac{\mathrm{k_B}T\log(t_\mathrm{s}/\tau_{0\mathrm{r}}) - \mu_\mathrm{cr}}{\sigma_\mathrm{cr}}, \frac{\sigma_\mathrm{cr}}{\sigma_\mathrm{er}}\right) \tag{17.84}$$

$$G_\mathrm{p}(t_\mathrm{r}, t_\mathrm{s}) = F\left(\frac{\mathrm{k_B}T\log(t_\mathrm{r}/\tau_{0\mathrm{p}}) - \mu_{\Delta\mathrm{ep}} - \mu_\mathrm{cp}}{\sigma_\mathrm{ep}}, \frac{\mathrm{k_B}T\log(t_\mathrm{s}/\tau_{0\mathrm{p}}) - \mu_\mathrm{cp}}{\sigma_\mathrm{cp}}, \frac{\sigma_\mathrm{cp}}{\sigma_\mathrm{ep}}\right), \tag{17.85}$$

where A_r and A_p give the maximum degradation obtainable from each peak. The limiting case of zero delay ($a \to -\infty$) is simply obtained as $F(a,b) = \Phi(b)$, in agreement with the discussion in Sect. 17.3.5.1.

If the experiment is carried out in an on-the-fly manner, we have zero delay ($a \to -\infty$). However, the degradation is measured relative to the value obtained after a certain measurement delay $t_\mathrm{s} = t_0$, see Fig. 17.7. Thus, we have

$$\Delta V_{\mathrm{th}}(0, t_\mathrm{s}) = A_\mathrm{r}\Big(G_\mathrm{r}(0, t_\mathrm{s}) - G_\mathrm{r}(0, t_0)\Big) + A_\mathrm{p}\Big(G_\mathrm{p}(0, t_\mathrm{s}) - G_\mathrm{p}(0, t_0)\Big). \tag{17.86}$$

Finally, for the calculation of AC stress with period T and a duty-factor γ we need the auxiliary integral (see Figs. 17.7 and 17.14)

$$F_\gamma(a,b_1,b_2,\rho) = \int_{-b_1}^{b_2} \mathrm{d}y \int_{-a\sqrt{1-\rho^2}+\rho y}^{\infty} \mathrm{d}x\, f(x,y,\rho)$$
$$= \int_{-b_1}^{b_2} \mathrm{d}y\, \phi(y)\, Q\Big(\frac{-a\sqrt{1-\rho^2}+\rho y-\rho y}{\sqrt{1-\rho^2}}\Big)$$
$$= (\Phi(b_2)-\Phi(b_1))\,\Phi(a), \tag{17.87}$$

which is fortunately very simple to calculate. With the auxiliary functions F and F_γ, the total ΔV_{th} can be constructed at any time of an AC stress sequence. For instance, at the end of the V_{L} period, where the recovery time is $t_{\mathrm{r}} = (1-\alpha)T$, we would have

$$\Delta V_{\mathrm{th}}((1-\alpha)T,t_{\mathrm{s}}) = A_{\mathrm{r}}\Big(G_{\mathrm{r}}((1-\alpha)T,\alpha T)+G_{\gamma\mathrm{r}}((1-\alpha)T,\alpha t_{\mathrm{s}})\Big)+$$
$$A_{\mathrm{p}}\Big(G_{\mathrm{p}}((1-\alpha)T,\alpha T)+G_{\gamma\mathrm{p}}((1-\alpha)T,\alpha t_{\mathrm{s}})\Big), \tag{17.88}$$

where $G_{\gamma\mathrm{r}}$ and $G_{\gamma\mathrm{p}}$ are defined analogously to G_{r} and G_{p}.

17.4.1 Bias Dependence

While the temperature dependence is inherently considered by the distribution of the activation energies, the bias dependence of the CET maps is modeled by assuming the amplitude of each component to follow $A = (V_{\mathrm{stress}}/V_{\mathrm{s0}})^m$, with the stress voltage V_{stress} and constants V_{s0} and m. Also, as previous studies on individual defects have shown [10], the mean values of the distribution are expected to approximately follow $\mu_{\mathrm{c}} = \mu_{\mathrm{c0}} + kV_{\mathrm{stress}}$ and $\Delta\mu_{\mathrm{e}} = \Delta\mu_{\mathrm{e0}} - kV_{\mathrm{stress}}$, with a constant k. The main effect of k is to shift the capture times toward shorter values without affecting the emission times. However, by fitting the model to experimental data, the effect of the bias on the mean values was found to be small and completely negligible for the permanent component, which is somewhat surprising given the strong exponential bias dependence of the individual defects.

17.4.2 Experimental Validation

Finally, the model is evaluated on a 2.2 nm SiON technology [95], where very detailed MSM data was acquired for the construction of the CET maps. Recording of each dataset required about 1–2 weeks. Figure 17.15 shows the analytic CET model, which contains all essential features visible in the numerical map shown in Fig. 17.6. In particular, the rightward slant of the distribution with increasing capture times, which previously necessitated the introduction of the higher-order polynomials for the mean and standard deviation of the single normal distribution [78], is

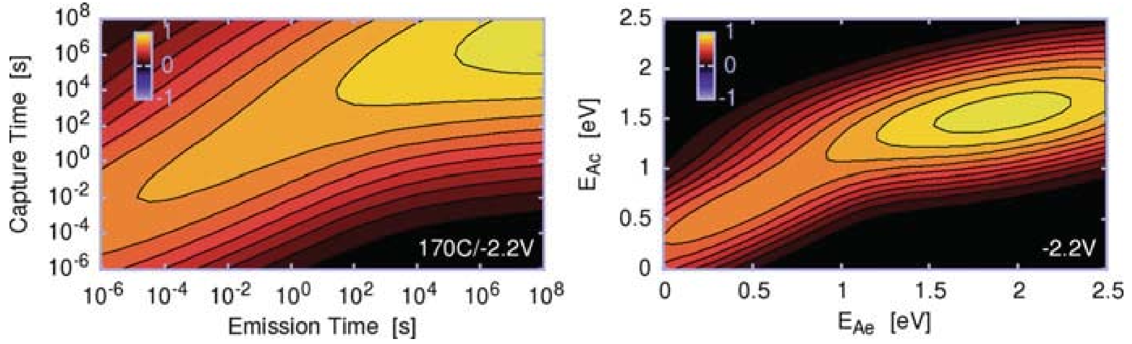

Fig. 17.15 *Left*: The analytic CET map extracted for the data shown in Fig. 17.16, which contains all essential features visible in Fig. 17.6. *Right*: The analytic activation energy map for the same data set

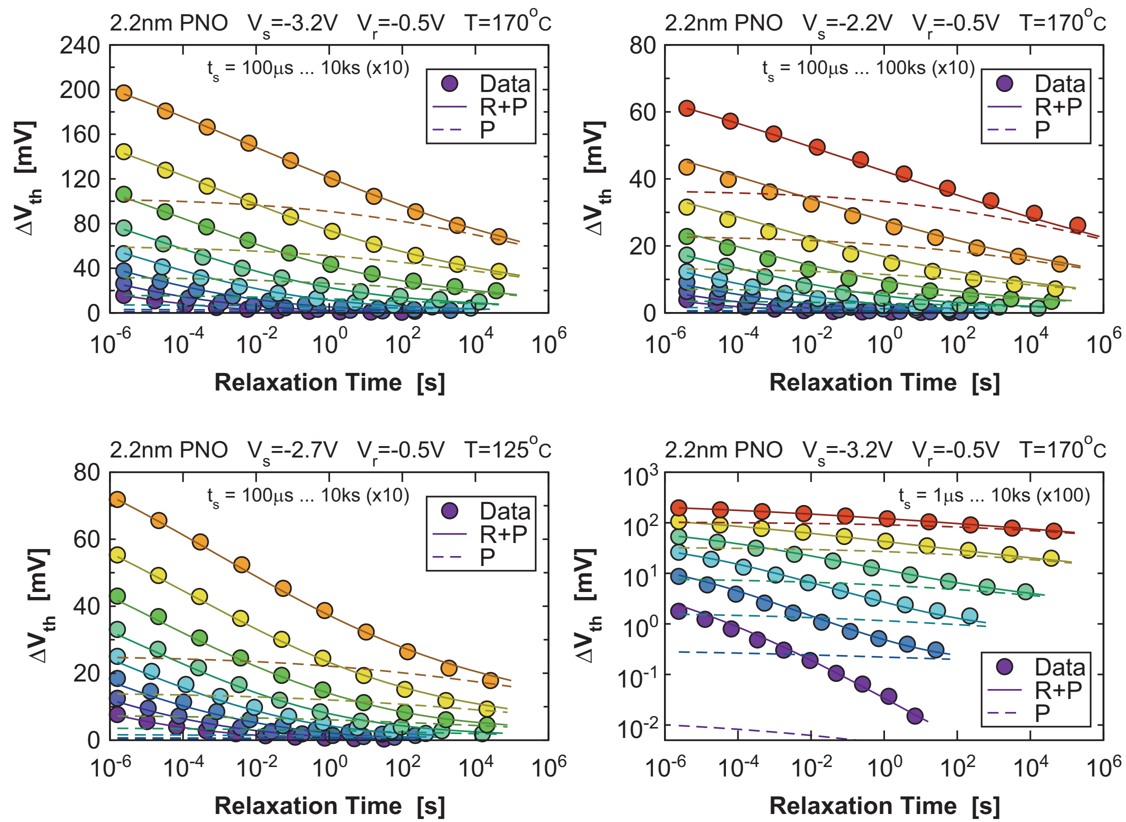

Fig. 17.16 Comparison of the analytic model using the activation energies of Fig. 17.15 to experimental data at different stress biases and temperatures. Excellent agreement is obtained for all stress and relaxation times in the extremely wide experimental window—also on a logarithmic scale (second column, *right-most figure*)

well captured by the superposition of two bivariate normal distributions. By simultaneously extracting the analytic distribution for a number of datasets recorded at different V_{stress} and T_{L}, a bias- and temperature-dependent analytic CET map is obtained. A convincing comparison of the analytic model to experimental data for a number of $V_{\text{stress}}/T_{\text{L}}$ combinations is given in Fig. 17.16 using the parameters of Table 17.1.

Table 17.1 Parameters used for the analytic CET maps of Figs. 17.15 and 17.16

	τ_0 (ns)	μ_c (eV)	σ_c (eV)	$\mu_{\Delta e}$ (eV)	$\sigma_{\Delta e}$ (mV)	V_{s0} (V)	m	k
R	98	0.55	0.43	−0.2	0.26	5.22	3.58	4.4×10^{-3} eV/V
P	0.59	1.6	0.31	0.32	0.48	3.04	3.74	0

17.5 Conclusions

Starting from a rigorous microscopic description of oxide defects and a somewhat less rigorous description of interface states, we have suggested a physics-based analytic model for BTI which covers DC, AC, and duty-factor dependent stress and the subsequent recovery as a function of stress voltage and temperature. Since the model is intuitively based on the occupancy of defects in the capture/emission time maps, it can be easily generalized to other more complicated stress/recovery patterns.

Acknowledgements This work would not have been possible without the invaluable support of B. Kaczer (imec) and H. Reisinger (Infineon Munich). Furthermore, inspiring discussions with W. Goes, P.-J. Wagner, and F. Schanovsky are gratefully acknowledged.

The research leading to these results has received funding from the FWF project n°23390-M24 and the European Community's FP7 project n°261868 (MORDRED).

References

1. M. Denais, V. Huard, C. Parthasarathy, G. Ribes, F. Perrier, N. Revil, and A. Bravaix, "Interface Trap Generation and Hole Trapping under NBTI and PBTI in Advanced CMOS Technology with a 2-nm Gate Oxide," *IEEE Trans.Dev.Mat.Rel.*, vol. 4, no. 4, pp. 715–722, 2004.
2. D.S. Ang, S. Wang, and C.H. Ling, "Evidence of Two Distinct Degradation Mechanisms from Temperature Dependence of Negative Bias Stressing of the Ultrathin Gate p-MOSFET," *IEEE Electron Device Lett.*, vol. 26, no. 12, pp. 906–908, 2005.
3. C.-T. Chan T. Wang AND, C.-J. Tang, C.-W. Tsai, H. Wang, M.-H. Chi, and D. Tang, "A Novel Transient Characterization Technique to Investigate Trap Properties in HfSiON Gate Dielectric MOSFETs—From Single Electron Emission to PBTI Recovery Transient," *IEEE Trans.Electron Devices*, vol. 53, no. 5, pp. 1073–1079, 2006.
4. V. Huard, M. Denais, and C. Parthasarathy, "NBTI Degradation: From Physical Mechanisms to Modelling," *Microelectronics Reliability*, vol. 46, no. 1, pp. 1–23, 2006.
5. S. Mahapatra, K. Ahmed, D. Varghese, A. E. Islam, G. Gupta, L. Madhav, D. Saha, and M. A. Alam, "On the Physical Mechanism of NBTI in Silicon Oxynitride p-MOSFETs: Can Differences in Insulator Processing Conditions Resolve the Interface Trap Generation versus Hole Trapping Controversy?," in *Proc. Intl.Rel.Phys.Symp. (IRPS)*, 2007, pp. 1–9.
6. J.P. Campbell, P.M. Lenahan, C.J. Cochrane, A.T. Krishnan, and S. Krishnan, "Atomic-Scale Defects Involved in the Negative-Bias Temperature Instability," *IEEE Trans.Dev.Mat.Rel.*, vol. 7, no. 4, pp. 540–557, 2007.
7. Th. Aichinger, M. Nelhiebel, S. Einspieler, and T. Grasser, "Observing Two Stage Recovery of Gate Oxide Damage Created under Negative Bias Temperature Stress," *J.Appl.Phys.*, vol. 107, pp. (024508–1)–(024508–8), 2010.

8. V. Huard, C. Parthasarathy, and M. Denais, “Single-Hole Detrapping Events in pMOSFETs NBTI Degradation,” in *Proc. Intl.Integrated Reliability Workshop*, 2005, pp. 5–9.
9. H. Reisinger, T. Grasser, and C. Schlünder, “A Study of NBTI by the Statistical Analysis of the Properties of Individual Defects in pMOSFETs,” in *Proc. Intl.Integrated Reliability Workshop*, 2009, pp. 30–35.
10. T. Grasser, H. Reisinger, P.-J. Wagner, W. Goes, F. Schanovsky, and B. Kaczer, “The Time Dependent Defect Spectroscopy (TDDS) for the Characterization of the Bias Temperature Instability,” in *Proc. Intl.Rel.Phys.Symp. (IRPS)*, May 2010, pp. 16–25.
11. V. Huard, “Two Independent Components Modeling for Negative Bias Temperature Instability,” in *Proc. Intl.Rel.Phys.Symp. (IRPS)*, May 2010, pp. 33–42.
12. M. Denais, V. Huard, C. Parthasarathy, G. Ribes, F. Perrier, D. Roy, and A. Bravaix, “Perspectives on NBTI in Advanced Technologies: Modelling & Characterization,” in *Proc. ESSDERC*, 2005, pp. 399–402.
13. D.S. Ang, “Observation of Suppressed Interface State Relaxation under Positive Gate Biasing of the Ultrathin Oxynitride Gate p-MOSFET Subjected to Negative-Bias Temperature Stressing,” *IEEE Electron Device Lett.*, vol. 27, no. 5, pp. 412–415, 2006.
14. Th. Aichinger, M. Nelhiebel, and T. Grasser, “Unambiguous Identification of the NBTI Recovery Mechanism using Ultra-Fast Temperature Changes,” in *Proc. Intl.Rel.Phys.Symp. (IRPS)*, 2009, pp. 2–7.
15. T. Grasser, Th. Aichinger, G. Pobegen, H. Reisinger, P.-J. Wagner, J. Franco, M. Nelhiebel, and B. Kaczer, “The ‘Permanent’ Component of NBTI: Composition and Annealing,” in *Proc. Intl.Rel.Phys.Symp. (IRPS)*, Apr. 2011, pp. 605–613.
16. W. Shockley and W.T. Read, *Physical Review*, vol. 87, no. 5, pp. 835–842, 1952.
17. A.L. McWhorter, “1/f Noise and Germanium Surface Properties,” *Sem.Surf.Phys*, pp. 207–228, 1957.
18. F.P. Heiman and G. Warfield, “The Effects of Oxide Traps on the MOS Capacitance,” *IEEE Trans.Electron Devices*, vol. 12, no. 4, pp. 167–178, 1965.
19. M. Masuduzzaman, A.E. Islam, and M.A. Alam, “Exploring the Capability of Multifrequency Charge Pumping in Resolving Location and Energy Levels of Traps Within Dielectric,” *IEEE Trans.Electron Devices*, vol. 55, no. 12, pp. 3421–3431, 2008.
20. T. Grasser, “Stochastic Charge Trapping in Oxides: From Random Telegraph Noise to Bias Temperature Instabilities,” in *Microelectronics Reliability*, 2012, vol. 52, pp. 39–70.
21. T. Grasser, H. Reisinger, W. Goes, Th. Aichinger, Ph. Hehenberger, P.J. Wagner, M. Nelhiebel, J. Franco, and B. Kaczer, “Switching Oxide Traps as the Missing Link between Negative Bias Temperature Instability and Random Telegraph Noise,” in *Proc. Intl.Electron Devices Meeting (IEDM)*, 2009, pp. 729–732.
22. T. Grasser, H. Reisinger, P.-J. Wagner, and B. Kaczer, *Physical Review B*, vol. 82, no. 24, pp. 245318, 2010.
23. A. Palma, A. Godoy, J. A. Jimenez-Tejada, J. E. Carceller, and J. A. Lopez-Villanueva, *Physical Review B*, vol. 56, no. 15, pp. 9565–9574, 1997.
24. J.F. Conley Jr., P.M. Lenahan, A.J. Lelis, and T.R. Oldham, “Electron Spin Resonance Evidence that E'_γ Centers can Behave as Switching Oxide Traps,” *IEEE Trans.Nucl.Sci.*, vol. 42, no. 6, pp. 1744–1749, 1995.
25. P.M. Lenahan and J.F. Conley Jr., “What Can Electron Paramagnetic Resonance Tell Us about the Si/SiO_2 System?,” *J.Vac.Sci.Technol.B*, vol. 16, no. 4, pp. 2134–2153, 1998.
26. C. Shen, M.-F. Li, X.P. Wang, H.Y. Yu, Y.P. Feng, A.T.-L. Lim, Y.C. Yeo, D.S.H. Chan, and D.L. Kwong, “Negative U Traps in HfO_2 Gate Dielectrics and Frequency Dependence of Dynamic BTI in MOSFETs,” in *Proc. Intl.Electron Devices Meeting (IEDM)*, 2004, pp. 733–736.
27. T. Yang, C. Shen, M.-F. Li, C.H. Ang, C.X. Zhu, Y.-C. Yeo, G. Samudra, S.C. Rustagi, M.B. Yu, and D.-L. Kwong, “Fast DNBTI Components in p-MOSFET with SiON Dielectric,” *IEEE Electron Device Lett.*, vol. 26, no. 11, pp. 826–828, 2005.
28. T. Grasser, B. Kaczer, H. Reisinger, P.-J. Wagner, and M. Toledano-Luque, “On the Frequency Dependence of the Bias Temperature Instability,” in *Proc. Intl.Rel.Phys.Symp. (IRPS)*, Apr. 2012, pp. XT.8.1–XT.8.7.

29. T. Grasser, H. Reisinger, K. Rott, M. Toledano-Luque, and B. Kaczer, "On the Microscopic Origin of the Frequency Dependence of Hole Trapping in pMOSFETs," in *Proc. Intl.Electron Devices Meeting (IEDM)*, Dec. 2012, pp. 19.6.1–19.6.4.
30. W. Goes, F. Schanovsky, and T. Grasser (2013) Advanced modeling of oxide defects. In: T. Grasser (eds) Bias temperature instability for devices and circuits. Springer, New York
31. B. Kaczer, T. Grasser, J. Martin-Martinez, E. Simoen, M. Aoulaiche, Ph.J. Roussel, and G. Groeseneken, "NBTI from the Perspective of Defect States with Widely Distributed Time Scales," in *Proc. Intl.Rel.Phys.Symp. (IRPS)*, 2009, pp. 55–60.
32. V.V. Afanas'ev and A. Stesmans, "Proton Nature of Radiation-Induced Positive Charge in SiO_2 Layers on Si," *Eur.Phys.Lett.*, vol. 53, no. 2, pp. 233–239, 2001.
33. J.P. Campbell, P.M. Lenahan, A.T. Krishnan, and S. Krishnan, "Identification of the Atomic-Scale Defects Involved in the Negative Bias Temperature Instability in Plasma-Nitrided p-Channel Metal-Oxide-Silicon Field-Effect Transistors," *J.Appl.Phys.*, vol. 103, no. 4, pp. 044505, 2008.
34. J.T. Ryan, P.M. Lenahan, T. Grasser, and H. Enichlmair, "Observations of Negative Bias Temperature Instability Defect Generation via On The Fly Electron Spin Resonance," *Appl.Phys.Lett.*, vol. 96, no. 22, pp. 223509–1–223509–3, 2010.
35. B. Kaczer, S. Mahato, V. Camargo, M. Toledano-Luque, Ph.J. Roussel, T. Grasser F. Catthoor, P. Dobrovolny, P. Zuber, G. Wirth, and G. Groeseneken, "Atomistic Approach to Variability of Bias-Temperature Instability in Circuit Simulations," in *Proc. Intl.Rel.Phys.Symp. (IRPS)*, 2011, pp. 915–919.
36. H. Reisinger, T. Grasser, K. Ermisch, H. Nielen, W. Gustin, and Ch. Schlünder, "Understanding and Modeling AC BTI," in *Proc. Intl.Rel.Phys.Symp. (IRPS)*, Apr. 2011, pp. 597–604.
37. T. Grasser, P.-J. Wagner, H. Reisinger, Th. Aichinger, G. Pobegen, M. Nelhiebel, and B. Kaczer, "Analytic Modeling of the Bias Temperature Instability Using Capture/Emission Time Maps," in *Proc. Intl.Electron Devices Meeting (IEDM)*, Dec. 2011, pp. 27.4.1–27.4.4.
38. K. Zhao, J.H. Stathis, B.P. Linder, E. Cartier, and A. Kerber, "PBTI Under Dynamic Stress: From a Single Defect Point of View," in *Proc. Intl.Rel.Phys.Symp. (IRPS)*, Apr. 2011, pp. 372–380.
39. J.P. Campbell and P.M. Lenahan(2013) Atomic scale defects associated with the negative bias temperature instability. In: T. Grasser (eds) Bias temperature instability for devices and circuits. Springer, New York
40. V.V. Afanas'ev, M. Houssa, A. Stesmans (2013) Charge properties of paramagnetic defects in semiconductor/oxide structures. In: T. Grasser (eds) Bias temperature instability for devices and circuits. Springer, New York
41. G. Groeseneken, H.E. Maes, N. Beltran, and R.F. de Keersmaecker, "A Reliable Approach to Charge-Pumping Measurements in MOS Transistors," *IEEE Trans.Electron Devices*, vol. 31, no. 1, pp. 42–53, 1984.
42. M.-F. Li, D. Huang, C. Shen, T. Yang, W.J., W.J. Liu, and Z. Liu, "Understand NBTI Mechanism by Developing Novel Measurement Techniques," *IEEE Trans.Dev.Mat.Rel.*, vol. 8, no. 1, pp. 62–71, March 2008.
43. Ph. Hehenberger, Th. Aichinger, T. Grasser, W. Goes, O. Triebl, B. Kaczer, and M. Nelhiebel, "Do NBTI-Induced Interface States Show Fast Recovery? A Study Using a Corrected On-The-Fly Charge-Pumping Measurement Technique," in *Proc. Intl.Rel.Phys.Symp. (IRPS)*, 2009, pp. 1033–1038.
44. M. Denais, A. Bravaix, V. Huard, C. Parthasarathy, C. Guerin, G. Ribes, F. Perrier, M. Mairy, and D. Roy, "Paradigm Shift for NBTI Characterization in Ultra-Scaled CMOS Technologies," in *Proc. Intl.Rel.Phys.Symp. (IRPS)*, 2006, pp. 735–736.
45. T. Grasser and B. Kaczer, "Negative Bias Temperature Instability: Recoverable versus Permanent Degradation," in *Proc. ESSDERC*, 2007, pp. 127–130.
46. Th. Aichinger, M. Nelhiebel, and T. Grasser, "A Combined Study of p- and n-Channel MOS Devices to Investigate the Energetic Distribution of Oxide Traps after NBTI," *IEEE Trans.Electron Devices*, vol. 56, no. 12, pp. 3018–3026, 2009.

47. T. Grasser, K. Rott, H. Reisinger, P.-J. Wagner, W. Goes, F. Schanovsky, M. Waltl, M. Toledano-Luque, and B. Kaczer, "Advanced Characterization of Oxide Traps: The Dynamic Time-Dependent Defect Spectroscopy," in *Proc. Intl.Rel.Phys.Symp. (IRPS)*, Apr. 2013.
48. T. Grasser, B. Kaczer, W. Goes, Th. Aichinger, Ph. Hehenberger, and M. Nelhiebel, "Understanding Negative Bias Temperature Instability in the Context of Hole Trapping," Microelectronic Engineering, 2009, 86, 7–9, pp. 1876–1882
49. T. Grasser and B. Kaczer, "Evidence that Two Tightly Coupled Mechanism are Responsible for Negative Bias Temperature Instability in Oxynitride MOSFETs," *IEEE Trans.Electron Devices*, vol. 56, no. 5, pp. 1056–1062, 2009.
50. S. Mahapatra, A.E. Islam, S. Deora, V.D. Maheta, K. Joshi1, A. Jain, and M.A. Alam, "A Critical Re-evaluation of the Usefulness of R-D Framework in Predicting NBTI Stress and Recovery," in *Proc. Intl.Rel.Phys.Symp. (IRPS)*, 2011, pp. 614–623.
51. A. Stesmans, *Physical Review B*, vol. 61, no. 12, pp. 8393–8403, 2000.
52. H. Reisinger (2013) The time dependent defect spectroscopy. In: T. Grasser (eds) Bias temperature instability for devices and circuits. Springer, New York
53. A.J. Lelis and T.R. Oldham, "Time Dependence of Switching Oxide Traps," *IEEE Trans.Nucl.Sci.*, vol. 41, no. 6, pp. 1835–1843, Dec 1994.
54. D.T. Gillespie, *Markov Processes: An Introduction for Physical Scientists*, Academic Press, 1992.
55. O.C. Ibe, *Markov Processes for Stochastic Modeling*, Academic Press, 2009.
56. K. Huang and A. Rhys, "Theory of Light Absorption and Non-Radiative Transitions in F-Centres," *Proc.R.Soc.A*, vol. 204, pp. 406–423, 1950.
57. C.H. Henry and D.V. Lang, *Physical Review B*, vol. 15, no. 2, pp. 989–1016, 1977.
58. A.M. Stoneham, "Non-radiative Transitions in Semiconductors," *Rep.Prog.Phys.*, vol. 44, pp. 1251–1295, 1981.
59. W.B. Fowler, J.K. Rudra, M.E. Zvanut, and F.J. Feigl, *Physical Review B*, vol. 41, no. 12, pp. 8313–8317, 1990.
60. B.K. Ridley, *Quantum Processes in Semiconductors*, Oxford University Press, third edition, 1993.
61. C.S. Kelley, *Physical Review B*, vol. 20, no. 12, pp. 5084–5089, 1979.
62. F. Schanovsky, W. Goes, and T. Grasser, "Multiphonon Hole Trapping from First Principles," *J.Vac.Sci.Technol.B*, vol. 29, no. 1, pp. 01A2011–01A2015, 2011.
63. A. Asenov, R. Balasubramaniam, A.R. Brown, and J.H. Davies, "RTS Amplitudes in Decananometer MOSFETs: 3-D Simulation Study," *IEEE Trans.Electron Devices*, vol. 50, no. 3, pp. 839–845, 2003.
64. S.M. Amoroso (2013) Statistical study of bias temperature instabilities by means of 3D atomistic simulation. In: T. Grasser (eds) Bias temperature instability for devices and circuits. Springer, New York
65. T. Nagumo, K. Takeuchi, T. Hase, and Y. Hayashi, "Statistical Characterization of Trap Position, Energy, Amplitude and Time Constants by RTN Measurement of Multiple Individual Traps," in *Proc. Intl.Electron Devices Meeting (IEDM)*, 2010, pp. 628–631.
66. T. Yang, C. Shen, M.-F. Li, C.H. Ang, C.X. Zhu, Y.-C. Yeo, G. Samudra, and D.-L. Kwong, "Interface Trap Passivation Effect in NBTI Measurement for p-MOSFET with SiON Gate Dielectric," *IEEE Electron Device Lett.*, vol. 26, no. 10, pp. 758–760, 2005.
67. T. Grasser, B. Kaczer, Th. Aichinger, W. Goes, and Michael Nelhiebel, "Defect Creation Stimulated by Thermally Activated Hole Trapping as the Driving Force Behind Negative Bias Temperature Instability in SiO_2, SiON, and High-k Gate Stacks," in *Proc. Intl.Integrated Reliability Workshop*, Apr. 2008, pp. 91–95.
68. M.A. Alam, H. Kufluoglu, D. Varghese, and S. Mahapatra, "A Comprehensive Model for pMOS NBTI Degradation: Recent Progress," *Microelectronics Reliability*, vol. 47, no. 6, pp. 853–862, 2007.
69. S. Mahapatra (2013) A comprehensive modeling framework for DC and AC NBTI. In: T. Grasser (eds) Bias temperature instability for devices and circuits. Springer, New York

70. T. Grasser, B. Kaczer, W. Goes, H. Reisinger, Th. Aichinger, Ph. Hehenberger, P.-J. Wagner, F. Schanovsky, J. Franco, M. Toledano-Luque, and M. Nelhiebel, “The Paradigm Shift in Understanding the Bias Temperature Instability: From Reaction-Diffusion to Switching Oxide Traps,” *IEEE Trans.Electron Devices*, vol. 58, no. 11, pp. 3652–3666, 2011.
71. F. Schanovsky and T. Grasser, “On the Microscopic Limit of the Modified Reaction-Diffusion Model for the Negative Bias Temperature Instability,” in *Proc. Intl.Rel.Phys.Symp. (IRPS)*, Apr. 2012, pp. XT.10.1–XT.10.6.
72. F. Schanovsky and T. Grasser (2013) On the microscopic limit of the RD model. In: T. Grasser (eds) Bias temperature instability for devices and circuits. Springer, New York
73. Y. Yang and M.H. White, “Charge Retention of Scaled SONOS Nonvolatile Memory Devices at Elevated Temperatures,” *Solid-State Electron.*, vol. 44, pp. 949–958, 2000.
74. Y. Gao, A.A. Boo, Z.Q. Teo, and D.S. Ang, “On the Evolution of the Recoverable Component of the SiON, HfSiON and HfO_2 P-MOSFETs under Dynamic NBTI,” in *Proc. Intl.Rel.Phys.Symp. (IRPS)*, Apr. 2011, pp. 935–940.
75. Z.Q. Teo, A.A. Boo, D.S. Ang, and K.C. Leong, “On the Cyclic Threshold Voltage Shift of Dynamic Negative-Bias Temperature Instability,” in *Proc. Intl.Rel.Phys.Symp. (IRPS)*, 2011, pp. 943–947.
76. M. Duan, J.F. Zhang, Z. Ji, W.D. Zhang, B. Kaczer, S. De Gendt, and G. Groeseneken, “Defect Loss: A New Concept for Reliability of MOSFETs,” *IEEE Electron Device Lett.*, vol. 33, no. 4, pp. 480–482, 2012.
77. D.S. Ang (2013) Understanding negative-bias temperature instability from dynamic stress experiments. In: T. Grasser (eds) Bias temperature instability for devices and circuits. Springer, New York
78. H. Reisinger, T. Grasser, W. Gustin, and C. Schlünder, “The Statistical Analysis of Individual Defects Constituting NBTI and its Implications for Modeling DC- and AC-Stress,” in *Proc. Intl.Rel.Phys.Symp. (IRPS)*, May 2010, pp. 7–15.
79. M. Toledano-Luque, B. Kaczer, Ph.J. Roussel, T. Grasser, G.I. Wirth, J. Franco, C. Vrancken, N. Horiguchi, and G. Groeseneken, “Response of a Single Trap to AC Negative Bias Temperature Stress,” in *Proc. Intl.Rel.Phys.Symp. (IRPS)*, 2011, pp. 364–371.
80. M. Denais, A. Bravaix, V. Huard, C. Parthasarathy, G. Ribes, F. Perrier, Y. Rey-Tauriac, and N. Revil, “On-the-fly Characterization of NBTI in Ultra-Thin Gate Oxide pMOSFET’s,” in *Proc. Intl.Electron Devices Meeting (IEDM)*, 2004, pp. 109–112.
81. A. Kerber and E. Cartier (2013) Bias temperature instability characterization methods. In: T. Grasser (eds) Bias temperature instability for devices and circuits. Springer, New York
82. H. Reisinger, O. Blank, W. Heinrigs, A. Mühlhoff, W. Gustin, and C. Schlünder, “Analysis of NBTI Degradation- and Recovery-Behavior Based on Ultra Fast V_{th}-Measurements,” in *Proc. Intl.Rel.Phys.Symp. (IRPS)*, 2006, pp. 448–453.
83. Ph. Hehenberger, P.-J. Wagner, H. Reisinger, and T. Grasser, “On the Temperature and Voltage Dependence of Short-Term Negative Bias Temperature Stress,” *Microelectronics Reliability*, vol. 49, pp. 1013–1017, 2009.
84. M.J. Kirton and M.J. Uren, “Noise in Solid-State Microstructures: A New Perspective on Individual Defects, Interface States and Low-Frequency (1/f) Noise,” *Adv.Phys.*, vol. 38, no. 4, pp. 367–486, 1989.
85. C. Shen, M.-F. Li, C. E. Foo, T. Yang, D.M. Huang, A. Yap, G.S. Samudra, and Y.-C. Yeo, “Characterization and Physical Origin of Fast V_{th} Transient in NBTI of pMOSFETs with SiON Dielectric,” in *Proc. Intl.Electron Devices Meeting (IEDM)*, 2006, pp. 333–336.
86. T. Grasser, W. Goes, V. Sverdlov, and B. Kaczer, “The Universality of NBTI Relaxation and its Implications for Modeling and Characterization,” in *Proc. Intl.Rel.Phys.Symp. (IRPS)*, 2007, pp. 268–280.
87. S. Rangan, N. Mielke, and E.C.C. Yeh, “Universal Recovery Behavior of Negative Bias Temperature Instability,” in *Proc. Intl.Electron Devices Meeting (IEDM)*, 2003, pp. 341–344.
88. T. Grasser, W. Goes, and B. Kaczer, “Towards Engineering Modeling of Negative Bias Temperature Instability,” in *Defects in Microelectronic Materials and Devices*, D. Fleetwood, R. Schrimpf, and S. Pantelides, Eds., pp. 399–436. Taylor and Francis/CRC Press, 2008.

89. G. Pobegen, T. Aichinger, M. Nelhiebel, and T. Grasser, "Understanding Temperature Acceleration for NBTI," in *Proc. Intl.Electron Devices Meeting (IEDM)*, Dec. 2011, pp. 27.3.1–27.3.4.
90. A. Haggag, W. McMahon, K. Hess, K. Cheng, J. Lee, and J. Lyding, "High-Performance Chip Reliability from Short-Time-Tests," in *Proc. Intl.Rel.Phys.Symp. (IRPS)*, 2001, pp. 271–279.
91. J.H. Cadwell, "The Bivariate Normal Integral," *Biometrica Trust*, vol. 38, no. 3/4, pp. 475–479, 1951.
92. R.J. Henery, "An Approximation to Certain Multivariate Normal Probabilities," *Journal of the Royal Statistical Society B*, vol. 43, no. 1, pp. 81–85, 1981.
93. D.R. Cox and N. Wermuth, "A Simple Approximation for Bivariate and Trivariate Normal Integrals," *International Statistical Review*, vol. 59, no. 2, pp. 263–269, 1991.
94. W.-J. Tsay and P.-H. Ke, "A Simple Approximation for Bivariate Normal Integral Based on Error Function and its Application on Probit Model with Binary Endogenous Regressor," *IEAS Working Paper No. 09-A011*, 2009.
95. T. Grasser, B. Kaczer, Ph. Hehenberger, W. Goes, R. O'Connor, H. Reisinger, W. Gustin, and C. Schlünder, "Simultaneous Extraction of Recoverable and Permanent Components Contributing to Bias-Temperature Instability," in *Proc. Intl.Electron Devices Meeting (IEDM)*, 2007, pp. 801–804.